Using Synchrotron Based X-Ray Imaging Technique to Understand Liquid Water Transport Phenomena in Proton Exchange Membrane (PEM) Fuel Cells

A Thesis Submitted to the College of Graduate and Postdoctoral Studies

in partial fulfillment of the requirements for the degree of

Master of Science

in the Department of Chemical and Biological Engineering

University of Saskatchewan

By

Paria Rahimian

Permission to Use

The author has agreed that the Libraries of the University of Saskatchewan may make this thesis freely available for inspection. Moreover, the author has agreed that permission for extensive copying of this thesis for scholarly purposes may be granted by the professor(s) who supervised the thesis work recorded herein or, in their absence, by the Head of the Department of Chemical and Biological Engineering or the Dean of the College of Graduate and Postdoctoral Studies. Copying or publication or any other use of the thesis or parts thereof for financial gain without written approval by the University of Saskatchewan is prohibited. It is also understood that due recognition will be given to the author of this thesis and to the University of Saskatchewan in any use of the material of the thesis.

Requests for permission to copy or to make other use of material in this thesis in whole or in part should be addressed to:

Head of the Department of Chemical and Biological Engineering

University of Saskatchewan

57 Campus Drive

Saskatoon, Saskatchewan

S7N 5A9

Canada

Abstract

Proton exchange membrane fuel cells (PEMFCs) are considered to be one of the most promising alternative power source for the automotive industry and stationary applications. However, proper water management in PEMFCs remains a challenge, hindering broader commercialization of this technology. Water as a by-product of this technology plays a complex role in the performance of a fuel cell. Too much water will flood the cell while too little water will dry the membrane. Both cases are not desired when operating fuel cells. Due to saturation and/or condensation, liquid water inevitably forms and the uniqueness is emergence of liquid water from the interconnected water pathways of gas diffusion layer (GDL) to gas flow channels. In flow channels, liquid water emerges in the form of droplets, growing to a critical size and becoming unstable. After detachment of unstable droplets, various gas-liquid flow patterns might occur alone or simultaneously along the channel depending on the operating conditions.

In this work, based on a force balance analysis an analytical approach was developed to predict which flow pattern is likely to occur under different operating conditions relevant to the fuel cell. It is found that the critical droplet size depends on the superficial gas velocity, contact angle and contact angle hysteresis of growing droplets. Also, the flow pattern assignment is influenced by the contact angle and contact angle hysteresis of droplets showing that increasing contact angle hysteresis leads to the slug flow regime.

The opaque nature of fuel cell components, including GDL materials, poses significant challenges to understand liquid transport in PEM fuel cells. In recent years, much attention has been placed on development of visualization techniques to detect liquid water and diagnose flooding problems in PEM fuel cells. In this study, an advanced synchrotron X-ray imaging

technique available at the Canadian Light Source (CLS) was employed for the first time to visualize liquid water transport in a PEM fuel cell under different operating parameters of relevance to fuel cell operation. Due to high spatial and temporal resolution coupled with high energy photons of the X-ray beam, synchrotron radiation can obtain high-resolution images of liquid water behaviour inside the GDL and gas flow channels of fuel cells. Using the X-ray images, evolution of droplets including emergence, growth, and detachment under different superficial gas velocities, was visualized and a cyclic pattern was obtained. In addition, the evolution of the height and chord of growing droplets as well as their dynamic contact angles were analyzed quantitatively. The critical droplet sizes were also observed from X-ray images. Increasing superficial gas velocity results in a decrease in the critical detachment diameter of the droplets. Also, the critical droplet size at detachment was compared to a simplified analytical model and there was good agreement between theoretical predictions and the experimental data.

Acknowledgments

First of all, I would like to express my gratitude to my supervisor, Dr. Lifeng Zhang, for giving me the chance to be a member of his research group and on top of that for his continuous support and guidance in overcoming numerous obstacles I have been facing through this challenging research.

I am also grateful to Dr. Ryan Anderson and Logan Battrell from Montana State University for their feedback and cooperation in this work which helped me to get results of better quality.

Also, I would like to thank my committee members, Dr. Wang from the Department of Chemical and Biological Engineering and Dr. Ning Zhu from Canadian Light Source (CLS), for providing me with valuable advice and suggestions during the research.

I also acknowledge the Dean's Scholarship received from the University of Saskatchewan and financial support from the Natural Sciences and Engineering Research Council of Canada (NSERC).

And finally, I would like to express my gratitude to all the members of the fluidization and particle characterization group, especially Milad Taghavivand, for all the useful discussion and suggestions.

Table of contents

List of tables

List of figures

Nomenclature

a_{Cho} Constant from Cho equation

b_{Cho} Constant from Cho equation

$2B$ Channel height (m)

$2b$ Channel height above a droplet (m)

D Droplet diameter (m)

D^{eff}_{dry} Effective diffusivity of a dry gas diffusion layer (m/s)

Da_0 Damkolher number, dimensionless

$f_{\mu,d}$ Viscous drag force (N)

f_i Force (N)

$2h$ Critical droplet height (m)

H Dimensionless droplet height

H_d Hydrodynamic diameter of channel (m)

l Distance from drop's upstream and downstream surface (m)

l^2 Projected area (m^2)

L Total channel length (m)

p_0' Upstream pressure over the droplet (Pa)

p_L' Downstream pressure over the droplet (Pa)

P Pressure (Pa)

r Radius (m)

R_0 Droplet radius (m)

Re Reynolds number, dimensionless

RH Relative humidity

u_g Superficial gas velocity (m/s)

u_L Superficial liquid velocity (m/s)

w Channel width (m)

We Weber Number, dimensionless

Greek letters

γ Surface tension (N/m)

μ Viscosity (Pa s)

θ_s Static contact angle (^{o})

θ_a Advancing contact angle (^{o})

θ_r Receding contact angle (^{o})

ρ Gas density (kg/m^3)

τ^{ω} Shear stress exerted by the gas flow (Pa)

Chapter 1 – Introduction

Proton exchange membrane fuel cells (PEMFCs) are regarded as a promising pathway to mitigate environmental and energy issues associated with fossil fuels. Also, they are expected to be one of the most efficient energy converters in portable power devices due to their high energy efficiency and environmental friendliness at the operation stage.

With hydrogen as their fuel, PEMFCs have increasingly been considered to be a possible solution to reduce greenhouse gas emissions particularly for the transportation sector[1]. However, successful utilization of fuel cells in stationary and mobile applications is dependent on properly addressing some challenging issues including water management.

Water is the main by-product of the fuel cell reaction which converts the chemical potential energy of the reactants into electrical energy. There are two reactant streams, a fuel (H_2) stream and an oxidant (O_2) stream that is readily available from the atmosphere. A typical fuel cell also contains two catalyst layers, two gas diffusion layers (GDLs), and two bipolar plates possessing several gas channels as indicated in Figure 1.1 below.

At the anode catalyst layer H_2 loses electrons to produce protons. Protons migrate through the membrane and electrons travel through the external circuit to generate electrical current. Afterwards, protons react with O_2 at the cathode catalyst layer with water and heat being generated. Water as the by-product will appear in liquid form due to saturation and condensation under typical fuel cell operating conditions. The liquid water appears from the GDL via capillary effect, accumulates in the gas flow channels, covers the GDL surface and increases the pressure drop along the channels. In addition to this, at low operating temperatures additional liquid water is

condensed on both sides. Therefore, liquid water becomes more problematic at low operating temperatures [2].

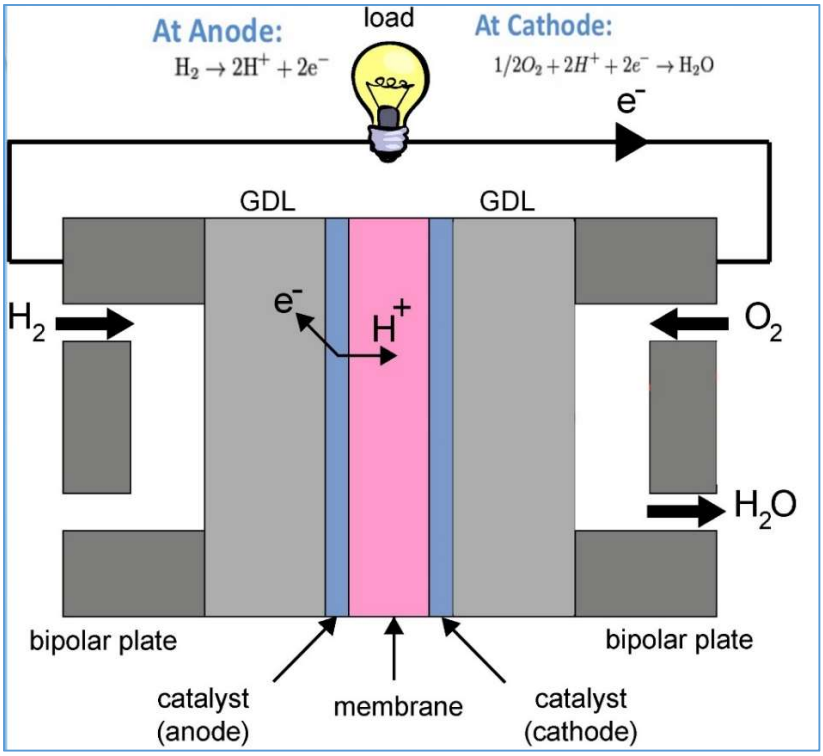

Figure 1.1 The water transport mechanism inside a PEM fuel cell (adopted from Ref [1]).

In general, a sufficient level of hydration is required to facilitate effective proton transport in the PEMFC. However, excess liquid water in fuel cells can cause many performance and durability problems, including flooding and blocking the pores of the catalyst layers, GDLs, and gas flow channels. Therefore, it is essential to keep a delicate balance between both too little and too much water content in a PEMFC since either a dry or flooded electrode adversely affects the performance and accelerates the degradation of the PEMFC in the long term [3].

Water content in PEMFCs is directly associated with the proton conductivity growth. Protons are surrounded by water molecules during the cell operation. As current is drawn from the anode to the cathode, water molecules are carried via protons moving through the membrane as well. This phenomenon, called electro-osmotic drag of water, along with electrochemical water production induces water flooding and water depletion at the cathode side and the anode side, respectively. Cathodic water accumulation, together with the concentration gradient between the anode and cathode side, cause water to diffuse towards the anode side and hinder membrane drying at the anode side. This phenomenon is called water back-diffusion. When the protonic current is low, water back-diffusion tends to overcome electro-osmotic drag, whereas at high current densities, electro-osmotic drag is likely to overcome back-diffusion which consequently causes the anode to dry out.

In general, poor water balance results in an inherent contradiction in cell operation which leads to reduced cell power output in PEMFCs. Too much water discharge causes severe membrane dehydration. It can result in inadequate ionic conductivity which prevents proton accessibility to the catalyst layer and induces temporary performance losses. Also, excessive water discharge can cause irreversible permanent damage to membranes, i.e. delamination and pinholes [4]. On the other hand, excessive accumulated water causes flooding in an operating fuel cell. Once flooding occurs, many problematic issues will occur including:

1- Flow channel blockage by accumulated liquid water that causes an increase in the pressure drop across the channel.
2- Irregular current distribution which affects the water production rate and thus water balance in an operating fuel cell.

3- Liquid film formation on GDLs and catalyst layers which restricts reactant gas transport to the reaction sites leading to a decrease in active sites of the catalyst [3].

Flooding is normally attributed to high ionic current density operation, when water formation rate is greater than the removal rate. However, Trabold et al. [5] reported that at low current densities due to the lower gas flow rates, there would be more water saturation in the flow channels. From their study, they found out that to prevail over more water production rate due to high current density, increasing the gas velocity would be sufficient. On the other hand, according to the results reported by Litster et al. [2], by increasing the cell temperature, flooding can be prevented even at high current densities because of internal heating which boosts the saturation pressure and evaporation rates.

In order to maintain good performance of fuel cells, flooding and membrane drying faults needs to be identified and proper consideration needs to be taken to wipe out the faults and thus hinders flawed operation and prevents probable damage. Since both mentioned water faults cannot be evaluated directly, an appropriate diagnostics method should be employed to monitor dynamic behavior of liquid water in GDLs and gas flow channels of the fuel cell.

1.1 Project motivation and knowledge gap

Despite significant attempts, water management in proton exchange membrane fuel cells (PEMFCs) still is a challenging issue. Most of previous studies on liquid water dynamics in gas flow channels of PEMFCs did not reveal how droplet instability results in various flow regimes after droplet detachment.

Additionally, the location and behaviour of droplets under different operating conditions are not exactly clear in gas flow channels of fuel cells. Direct optical imaging could be utilized to visualize droplet dynamics through a transparent plate from the top-view. However, to visualize the evolution of a growing droplet, particularly regarding dynamic contact angles and critical diameter of droplets, side view access is required. Droplets tend to emerge from random locations in serpentine or parallel channels. Therefore, direct optical imaging from the side view is not possible because of overlapping of parallel or in serpentine channels. For the same reason, capturing simultaneous occurrence of various flow patterns along the serpentine channels is not feasible either.

Synchrotron based X-ray imaging techniques can address this problem by offering the advantage of providing high energy penetrating photons plus high spatial and temporal resolution. Using X-ray images, regions with accumulated water in a serpentine channel can be detected. The X-ray imaging techniques are mainly performed to visualize liquid water in two major components of a PEM fuel cell: the gas flow channels and the porous gas diffusion layers (GDLs). Especially, using X-rays for the latter is of greater importance since peering into complex porous materials is not otherwise possible using direct optical imaging techniques. This cutting-edge visualization technique offers the advantage of capturing X-ray computed tomography (CT) images. CT images make one able to detect complex features of porous gas diffusion layers which can influence water transport through the interconnected pores of GDL.

Despite a few attempts of utilizing synchrotron X-ray imaging to understand water transport in PEMFCs, time dependent droplet behavior specifically in terms of droplet growth cycles and evolution of dynamic contact angles still require attention. Specifically, contact angle hysteresis of

growing droplets is a key parameter for simulations and simplified modeling where static contact angles are usually used.

1.2 Research objectives

In view of the knowledge gap discussed above, the primary objective of the thesis research was to provide qualitative analysis of the flow patterns formed in active fuel cells according to the literature data from operating PEMFCs under different operating conditions.

Another objective of this research was to understand droplet dynamics utilizing X-ray visualization techniques to provide information on the evolution of dynamic contact angles during a droplet growth cycle.

1.3 Organization of the thesis

The work presented in this thesis resulted in one publication and one manuscript under review. The thesis is written in the manuscript (paper) based style and organized into five chapters. The introduction is presented in Chapter 1, along with knowledge gap, objectives and thesis organization. In Chapter 2, literature review provides some background on dynamic behavior of liquid water, contact angles, droplet detachment diameter, flow patterns, visualization of liquid water, and two-phase flow studies in a PEM fuel cell.

Chapter 3 contains the first manuscript which presents an analytical solution to predict different flow regimes in PEM fuel cells. Based on the second manuscript, time dependent droplet dynamics on porous fuel cell material using synchrotron based X-ray imaging technique is presented in Chapter 4. Finally, a summary of results, conclusions and recommendations are presented in Chapter 5. In this work, the references are provided at the end of the associated chapter.

1.4 References

[1] A. Bazylak, Liquid water transport in fuel cell gas diffusion layers, PhD thesis, University of Victoria, (2008).

[2] S. Litster, C. R. Buie, T. Fabian, J. K. Eaton, and J. G. Santiago, Active Water Management for PEM Fuel Cells, J. Electrochem. Soc. 154 (2007) B1049–B1058.

[3] R. Anderson, L. Zhang, Y. Ding, M. Blanco, X. Bi, and D. P. Wilkinson, A critical review of two-phase flow in gas flow channels of proton exchange membrane fuel cells, J. Power Sources. 195 (2010) 4531–4553.

[4] A. Bazylak, Liquid water visualization in PEM fuel cells: A review, Int. J. Hydrogen Energy. 34 (2009) 3845–3857.

[5] T. A. Trabold, J. P. Owejan, D. L. Jacobson, M. Arif, and P. R. Huffman, In situ investigation of water transport in an operating PEM fuel cell using neutron radiography: Part 1 - Experimental method and serpentine flow field results, Int. J. Heat Mass Transf. 49 (2006) 4712–4720.

Chapter 2 – Literature review

In the following section, reviews of the main characteristics of gas-liquid flow in the PEMFC gas flow channels are provided. This includes the dynamic behavior of liquid water, two-phase flow patterns, different visualization techniques and two-phase pressure drop along with the gas flow channels.

2.1 Dynamic behavior of liquid water

For broader commercial implementation of fuel cell stacks, water management is one of the pivotal engineering challenges. Although several theoretical and experimental attempts have led to advances in some water management techniques, the dynamics of water transport including droplet emergence, growth and detachment is not well understood. This results from challenging modelling of complicated gas-liquid flow systems together with the opaque and optically inaccessible nature of fuel cell material that makes the direct observation of the liquid water transport process demanding. Figure 2.1 illustrates schematic droplet generation and further entering gas flow channel through the pores of the GDL.

Bazylak et al. [7] visualized the dynamics of droplet emergence, growth and detachment from the GDL surface utilizing fluorescence microscopy. They observed that the location of emerging droplets was random and varied by time. This observation supported the model of interconnected water pathways in GDL which was proposed in the same study.

After a droplet is introduced through the interconnected pores of the GDL, a variety of phenomena were observed in fuel cell channels including sporadic and random emergence of water droplets, film and slug flow formation and ultimately channel blocking.

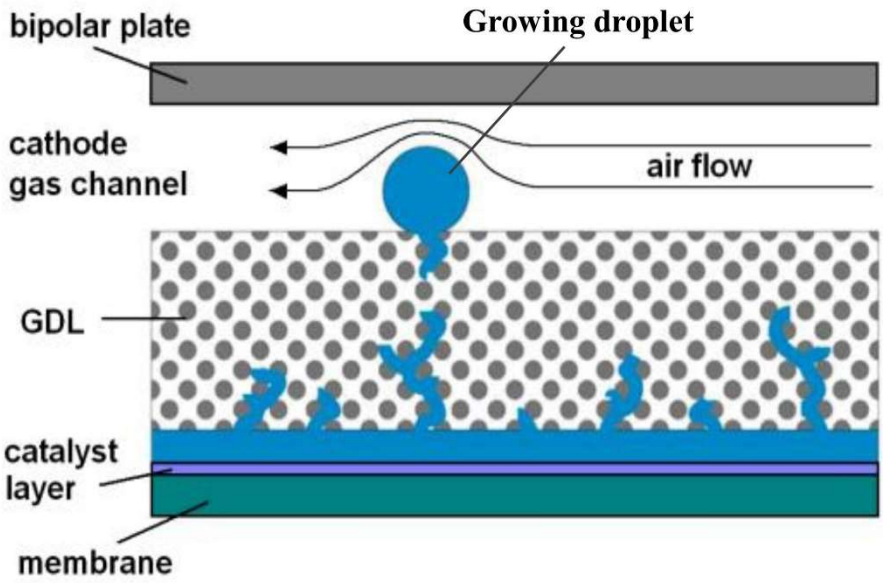

Figure 2.1 Droplet generation and entering gas flow channel through the pores of GDL (adopted from Ref [6]).

Yang et al. [8] observed the dynamics of droplet emergence and reported several preferential locations for emerging droplets through the water pathways of GDL. Chen et al. [9] predicted the onset of droplet instability in gas flow fields using a force balance model which was supported by optical visualizations. In order to simulate the droplet emergence phenomena, simplified spherical-droplet and cylindrical-droplet models were assumed. They suggested several modifications to facilitate liquid water removal including increasing channel length, decreasing channel height, and increasing superficial gas velocity.

In experimental investigations performed by Hidrovo et al. [10], liquid water in hydrophobic micro-channels was in the form of pancake-like slugs instead of spherical cap droplets due to the aspect ratio and geometry of the channels.

2.2 Contact angle

The contact angle of liquid water is a quantitative measure of the ability of liquid water for wetting a solid surface. It is dependent on thermodynamic equilibrium between three phases: droplet (liquid phase), substrate (solid phase) and atmosphere (gas phase). In water management studies, the contact angle is a key parameter which influences many dominant properties including adhesion force, capillary pressure, drag force and droplet shape deformation [11]. The drag force exerted by a gas flow deforms growing droplets that are pinned to the GDL surface via adhesion force.

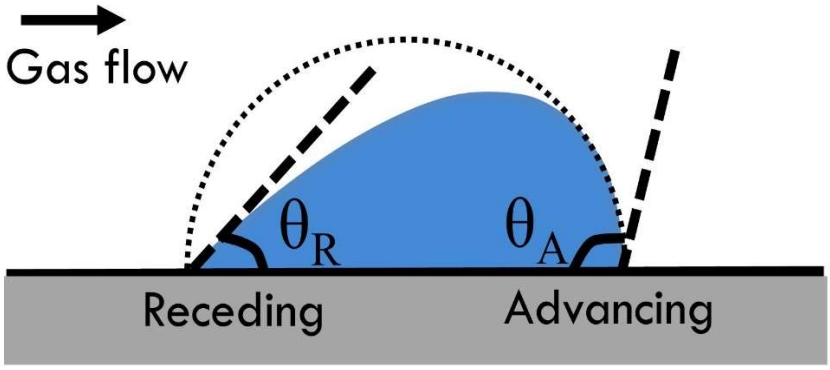

Figure 2.2 Advancing and receding contact angles made by a droplet as shown by θ_A and θ_R, respectively.

Figure 2.2 illustrates a schematic representation of a droplet on a solid surface while it is in advancing equilibrium. The maximum and minimum contact angles before the solid-liquid contact line of the droplet begins moving are termed as advancing and receding contact angles, respectively. The difference between θ_A and θ_R is termed as contact angle hysteresis which is a key factor in characterizing surface adhesion force and droplet instability [12]. Increasing superficial gas velocity results in an increase in contact angle hysteresis and leads the droplet into an unstable condition [13].

Kumber et al. [12] measured contact angle hysteresis of droplets sitting on GDLs with different polytetrafluoroethylene (PTFE) contents utilizing optical visualization. They observed that droplets growing on high PTFE loaded GDLs became more unstable and could get purged out more easily.

2.3 Droplet detachment diameter

There are two modes of liquid water removal from gas flow channels depending on superficial gas velocity. At high gas velocities, droplet detachment is by the shear force exerted by gas flow while at low gas velocities, the mechanism of water removal is by corner flow through capillary wicking of liquid water into the hydrophilic channel walls [13].

Several research groups have studied the droplet detachment mechanism by using a force balance analysis and considering all forces are experienced by a droplet sitting on a smooth solid surface[12]–[16]. Figure 2.3 indicates three forces are experienced by a droplet including the gravitational force (F_G), the adhesion force (F_A), and the drag force (F_D).

The drag force exerted by gas flow tries to make the droplet unstable and ultimately detach it from the GDL surface, whereas the surface adhesion force adheres the droplet on the surface. When the drag force prevails over the surface adhesion force droplet detachment takes place.

If the diameter of the detaching droplet is larger than the channel dimensions, then the gas flow channel will be blocked, flooding will occur and eventually it might shut down the fuel cell [13].

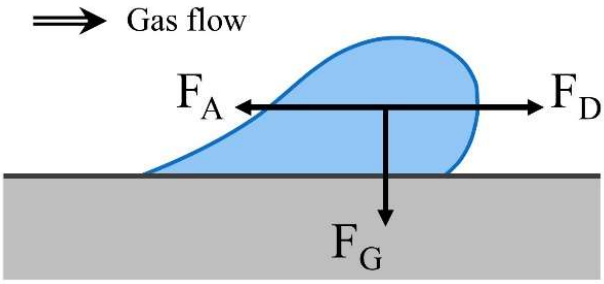

Figure 2.3 Forces applied to a droplet sitting on a smooth solid surface.

On the other hand, a larger amount of parasitic power is needed for supplying gaseous reactants at similar gas velocity in over-sized gas flow fields and this decreases fuel cell energy efficiency. Therefore, the critical detachment diameter of droplets is a key factor for designing gas flow channels of PEM fuel cells [11]. Mortazavi et al. [11] investigated the effect of several variables on the critical diameter of droplets upon detachment. Using optical visualization, they showed that by increasing PTFE content of GDL, due to higher capillary pressure, droplet detachment diameter decreased. Hence, small droplets without water clusters underneath to keep them adhered detached easily from the GDL surface. Also, they found that by increasing superficial gas velocity the larger drag force applied to the droplet made the critical detachment diameter smaller.

A relationship between superficial gas velocity and critical detachment diameter of growing droplets was proposed by Zhang et al. [13] using a force balance model. They found that by increasing the gas velocity, smaller droplets were capable of detaching from the GDL surface. Independently of the Zhang et al. [13] research group, Theodorakakos et al. [16] also found a correlation between the critical diameter of droplets and the gas velocity using computational fluid dynamics (CFD) simulations with a volume of fluid (VOF) method. They observed water droplet

behavior located on several different GDLs and measured dynamic contact angles of droplets at the moment of detachment.

After droplets grow to the critical diameter and detach from the GDL surface, their interactions with the channel side walls results in complex gas-liquid two phase flow patterns. The resulting flow patterns may vary throughout the gas flow channel depending on several factors, which are explained in detail below.

2.4 Flow patterns

Flow patterns observed in the fuel cell are found to be in the form of single phase flow, droplets, films, and slugs. The following is a brief description of the different flow patterns as summarized by Pei et al. [17]. During single-phase flow which occurs within the first moments after fuel cell operation, hardly any droplets can be detected on the GDL surface and the flow is mostly in the form of very small droplets tending to be evaporated quickly into the gas flow. Subsequently, during droplet flow, due to the electrochemical process of water production and vapor condensation, large droplets appear on the GDL and remain on its surface due to surface tension forces. As a result of the hydrophobic nature of PTFE loaded GDL material, droplets form a round shape and do not spread out laterally on the surface in contrast to film flow [18].

Once many droplets adhere to the surface, they coalesce and droplet flow transitions into film flow of growing thickness. As explained by Hussaini et al. [19], there is a constant inflow of water during cell operation and a wavy motion can be detected on the surface of film flow. Finally, when the film grows to a critical thickness any further growth leads to formation of a slow-moving slug flow, which is the main reason for oscillations in the pressure drop across the channels. Figure

2.4 shows different flow patterns in flow field channels of an active fuel cell. Blocking of the cross section of the channels may happen when large slugs form near the exit area of the gas flow channels and partially hinder the transport of gaseous reactants. Thus, local flooding might take place.

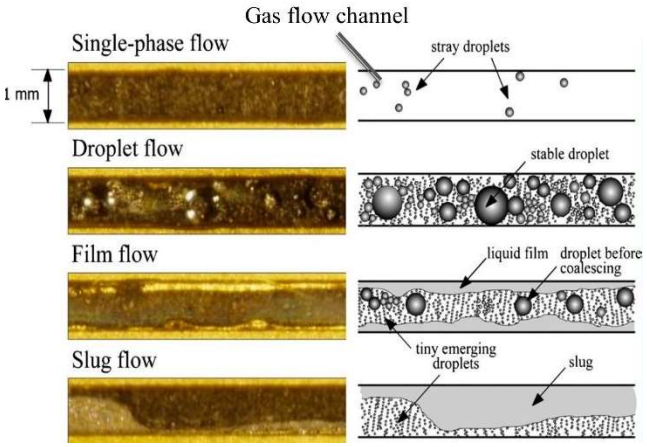

Figure 2.4 Various flow patterns in gas flow channels of an active fuel cell (adopted from Ref [3]).

Colosqui et al. [20] observed that the layer of residual water of previous slugs on the GDL could change the wetting properties of the surface and act as a pinning site influencing the dynamics of subsequent slug formation. They also found that the size of the slugs and the resulting pressure drop along the channel depended on the geometry of the channel and the interfacial forces. Günther et al. [21] observed three fundamentally different flow patterns including slug, bubbly and annular flow in micro-sized gas flow channels with a rectangular the cross section. Presenting an experimental flow map, they illustrated that the formation of the observed flow patterns was a function of the superficial gas and liquid velocities. Also, Kim et al. [21] noted that the cross-sectional shape of the gas flow channels was a key factor for prediction of the gas-liquid the flow patterns based on the flow pattern maps. By changing the geometry of the injection ports of the

channels, they identified several flow regimes, i.e. annular, segmented and capillary bubbly flow. They also found that changing the microchannel materials could influence two-phase pressure drop for capillary bubbly and segmented flow regimes. Note that bubbly (or capillary bubbly) flow pattern identified in these studies due to extremely high liquid to gas ratio (liquid phase dominated) is not probable to occur in operating fuel cells.

In the case of microfluidic applications, gas-liquid flow patterns relevant to fuel cell operating conditions are mainly in the form of droplet, film and slug flow. However, transition boundaries might vary depending on the GDL characteristics such as wettability and roughness. These flow regimes may take place solely or simultaneously at random locations along the channel [22].

2.5 Visualization of liquid water

In the literature, several diagnostic tools have been exploited to detect and characterize water distribution and two-phase flow including cell voltage, pressure drop measurements and visualization techniques. In recent years, several novel techniques have been utilized to visualize the liquid water formation in fuel cells by conducting either ex situ or in situ experiments. In situ visualization of liquid water behavior in gas flow channels of operating fuel cells is challenging due to the opaque nature of the fuel cell material which is mainly graphite. While, direct optical visualization is capable of capturing high spatial and temporal resolution images from liquid water on the surface of GDLs, beam interrogation visualization techniques can make observation of liquid water dynamics through GDL water pathways feasible.

In the following section, a brief overview is provided for commonly used visualization methods including nuclear magnetic resonance (NMR), direct optical photography, neutron imaging and synchrotron based X-ray imaging. Intrinsic strengths and limitations of each technique will be briefly discussed as well.

2.5.1 Nuclear magnetic resonance (NMR)

NMR imaging, also known as magnetic resonance imaging (MRI), provides inherently three-dimensional, high contrast images from opaque materials. Unlike direct optical photography, in this method the presence of liquid water can be detected under the GDL and land areas. However, the NMR technique is incompatible with conductive materials including carbon, thus it is limited in spatial and temporal resolution [23].

In 2004, Tsushima et al. [4] investigated the spatial distribution of liquid in a PEMFC employing the NMR imaging technique. According to their results, water content and pressure drop were inversely proportional to the output current density of the cell at steady-state operation. Additionally, due to the effect of electroosmotic drag, the majority of droplets emerged at the cathode side in comparison with the anode side. In 2005, in a separate work the same group again used NMR imaging to study cell performance by supplying water directly to the membrane. NMR images showed a membrane deformation at the location of water contact which they related to localized swelling of a PEM. They also reported that due to direct water supply lower membrane residence led to an increase in the cell voltage [24]. Feindel et al. [25] employed hydrogen deuterium exchange to increase the contrast in NMR images and investigate the difference in liquid water distribution under steady state conditions. Figure 2.5 shows their HNMR microscopy images

from membrane electrode assembly (MEA) and the gas flow channels. They also noted that the gas flow configuration was a key parameter that impacts the cell performance.

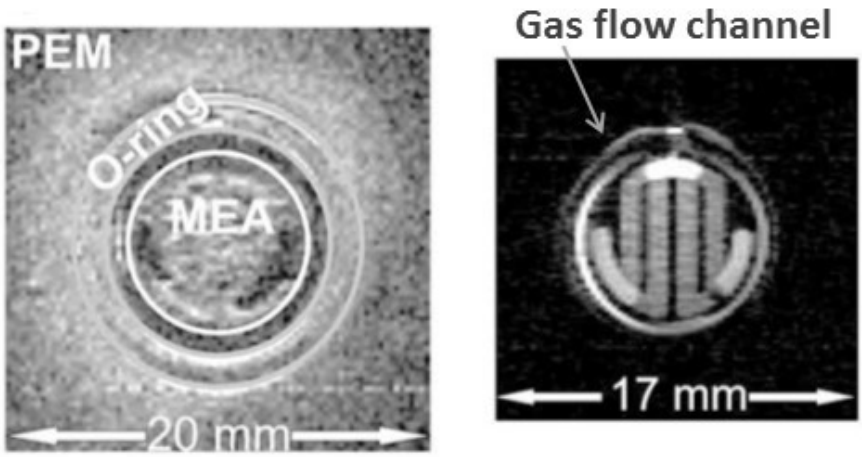

Figure 2.5 – HNMR microscopy images from PEMFC channels produced by Feindel et al. [26] left: 500 mm slice image showing membrane electrode assembly (MEA), right: 750 mm slice image showing liquid water accumulation in gas flow channels (adopted from [26]).

2.5.2 Optical photography

In order to employ direct optical photography to observe liquid water dynamics in an operating PEMFC, development of transparent fuel cell components is required. In this method, it is required to replace actual materials by transparent ones, resulting in changes in thermal conductivity and surface characteristics. Hence, material replacement is regarded as a drawback for optical photography.

Because of the opaque nature of GDL material, optical access to the pores of GDL is limited. Unlike the previous methods, it has advantages of providing high spatial and temporal resolution images. Using this method, researchers can visualize localized two-phase flow dynamics in the flow channels. This advantage makes optical photography compatible with operating fuel cells.

Spernjak et al. [27] also explored the level of efficiency of different GDL materials for water removal under different operating conditions. They demonstrated that the probability of water stagnation and subsequent poor cell performance was higher in hydrophobic GDLs. Also, they mentioned the importance of adding a microporous layer (MPL) to GDLs which makes a pressure barrier for water accumulation in the cathode but causes flooding in the anode side.

2.5.3 Neutron imaging

When performing neutron imaging, sample is bombarded with a neutron beam. The resulting attenuated signal provides information about the composition of sample material. Since neutron is sensitive to water molecule which is a hydrogen containing compound, this visualization technique particularly works in PEM fuel cells. On the downside, because of expensive technology and restricted accessibility of neutron imaging, this method is not wildly used throughout the world and it is only available for very few research groups.

Pekula et al. [28] observed liquid water behavior in gas flow channels using neutron imaging and reported that liquid water tended to accumulate at 90° bends in the channels. They considered the change in the momentum of gas flow as a result of this phenomena. Zhang et al. [29] compared the impact of using different GDL materials on liquid water accumulation at the cathode side using neutron imaging. They found that using carbon papers caused more water accumulation in the single channel compared to that with carbon cloth. Turhan et al. [30] used neutron imaging to compare the effect of numbers of channel-GDL interfaces on the water content in the gas flow channels of the fuel cell at a current density of 0.2 A/cm^2. They found that by increasing the channel-GDL interfaces, more liquid water was accumulated in the cell.

2.5.4 Synchrotron and X-ray imaging

X-ray tomography and synchrotron radiography are unique methods that allow in situ visualization of water transport behavior in an operating PEMFC through materials that would otherwise be opaque to optical access. In this method, a fuel cell is exposed to the direct X-ray beam and by traveling further in the cell, the beam intensity becomes attenuated. The transmitted X-ray beam is then processed to produce a three-dimensional structure of adsorption variation within the cell. Due to the higher transmission of high energy X-ray photons, this system offers the advantage of traversing and indicating details of GDL materials that cannot be obtained from optical visualization methods. Up to now, much effort has been devoted to visualizing liquid water evolution in PEMFCs [4]. Manke et al. [31] investigated in situ liquid water formation and transportation in a PEMFC using synchrotron X-ray radiography. They analyzed dynamic behavior of droplets inside the GDL and validated their previous findings in modeling and simulation by employing this novel technique. The same group also investigated the water distribution and multiphase flow phenomena in the cross-section of PEMFCs. They pointed out that water formation in the GDL depended on the water production rate that was closely linked to current density. Hence, due to the back diffusion at high current densities, droplets formed on the GDLs of both the anode and cathode sides [32]. Lee et al. [33] investigated the effect of using MPL on water transportation via synchrotron based X-ray imaging. Through-plane images indicate that applying MPL along with GDL improves the performance and efficiency of the PEMFC under wet operating conditions. Nano-sized pores of MPL help to hinder water cluster formation in GDL and prevent subsequent flooding in flow channels. Sasabe et al. [34] investigated the impact of the microstructure of the porous layer in a fuel cell on water accumulation and discharge behavior in the gas flow channels using X-ray radiography. Figure 2.6 illustrates X-ray images showing the

droplet growth at the interface between the catalyst layer and the GDL over time at the current density of 0.8 Acm^{-2}. They compared water transport through carbon cloth and carbon paper GDLs and found out that carbon cloth GDL performs better at high current density since liquid water tends to concentrate at the weaves of fiber bundles of carbon cloth. Hence, liquid water can get discharged easily to the gas flow channels.

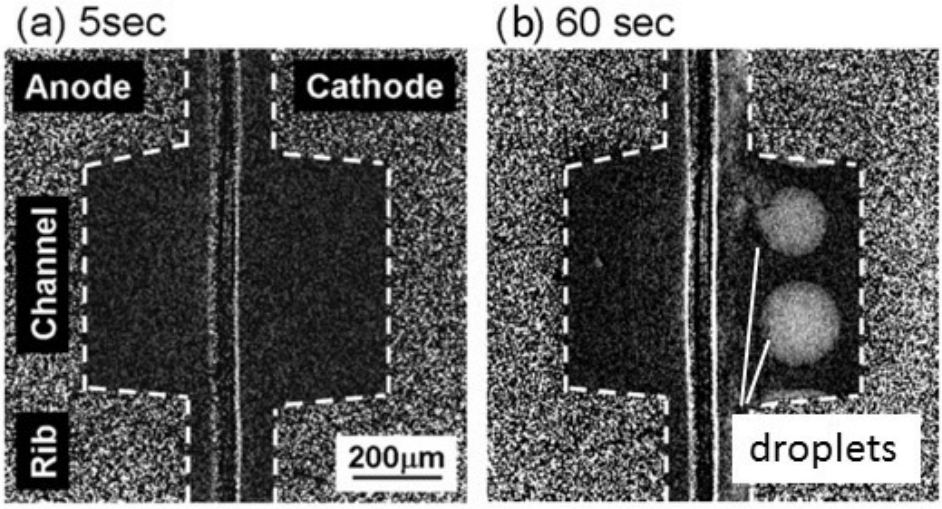

Figure 2.6 X-ray images showing liquid water accumulation at the interface between catalyst layer and GDL after a) 5 s and b) 60 s after the initiation of power generation at the current density of 0.8 A cm^{-2} (adopted from Ref [34]).

2.6 Two-phase flow studies in a PEM fuel cell

The presence of liquid water leads to two-phase flow in PEMFCs, which is different from that in conventional applications. Firstly, the gas to liquid flow ratio of two-phase flow in PEMFCs is high. The second distinction is the method of liquid introduction. Due to constant electrochemical water production, water content varies along the length of the flow channels and thus liquid water production rate and discharge should be taken into consideration. Thirdly, the location of newly generated droplets is totally random as droplet formation might occur on the

GDL surface toward the center or walls of the channel due to different contact angles of the flow field and the GDL material. Furthermore, after the droplets detach from the GDL surface, they join other droplets down the flow channel forming major droplets or slugs. For characterizing two-phase flow and the degree of flooding in PEMFCs, the pressure drop associated with water accumulation in the cell is utilized as a good diagnostic tool.

2.6.1 Pressure drop characteristics

Pressure drop in PEMFCs is the difference between the pressure of inlet and outlet of reactant and it depends on the amount of liquid water hold up in the flow channels [17]. As it is shown in Figure 2.7, when liquid water accumulates in the channel the pressure drop increases accordingly.

He et al. [35] used pressure drop between the inlet and outlet of channels to monitor the water saturation level and predict the flooding in PEMFC. Liu et al. [36] observed two-phase flow and pressure drop characteristics at both the anode and cathode sides of the cell. The effect of the fuel cell temperature, current density and operation time on pressure drop and cell performance were explored. Results provided direct evidence to show that water formation adversely influenced the mass transport followed by decreased performance of the PEMFC.

Investigating pressure drop across the flow channels is essential for optimizing power consumption and overall cell performance due to its direct effect on cost and sizing of PEMFC subsystems. Excess liquid water saturation and consequent flooding affects the gas flow, even possible to shut it down. As a result, it creates more parasitic power demand to pump air through the cells. Hence, minimizing pressure drop in flow channels is crucial as excessive pumping power decreases the maximum performance of the system [1].

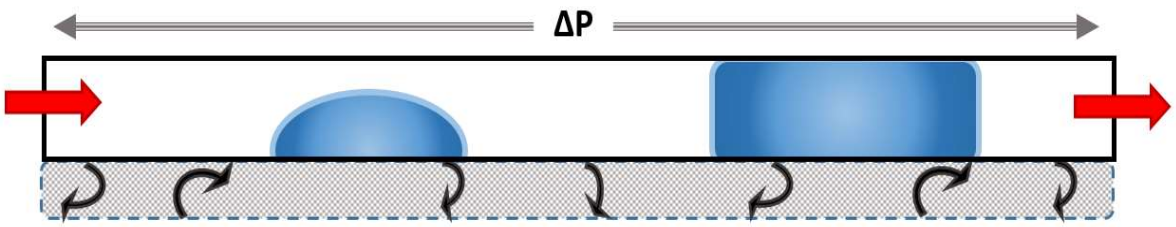

Figure 2.7 Schematic of water transport and corresponding pressure drop across the droplet in a gas flow channel.

In addition, pressure drop has been known as a practical diagnostic tool to quantify water content in the cell by comparing the cathodic pressure drop to the voltage which is indicative of the cell performance. This approach can be beneficial to predict cell flooding at both the cathode and anode sides where significant and slight flooding takes place. Pressure drop fluctuation at the anode side is not as much as at the cathode. However, any slug removal is followed by the spikes in the pressure signal observed at both sides [38]. In addition, the pressure difference between the cathode and anode side can be exploited to measure the level of water saturation in the GDL indicating the amount of liquid water transported into the flow channel [3]. Ma et al. [35] demonstrated that pressure drop measurements were capable of finding the best possible air velocity for water discharge at a given current density to optimize fuel cell operation. They also found a correlation between stagnant water and pressure drop fluctuations from pressure drop curves.

Pressure drop measurements can also be advantageous to develop a better understanding of two-phase flow mal-distribution along the parallel gas flow channels of a fuel cell, which is explained in detail in the following section.

2.6.2 Two phase flow mal-distribution

Two phase flow mal-distribution in parallel flow channels where water and air are introduced from a common inlet is quite a problem. Uniform reactant distribution is desirable in fuel cell operation since it can ensure uniform distribution of current density, temperature and water production. In contrast, non-uniform distribution results in either flooding or drying regions which create erratic fluctuations in pressure drop and consequently overall performance degradation [3].

Moreover, two phase flow instabilities reduce the operating lifetime of the cell due to localized hot spots in the membrane and subsequent material degradation. Therefore, proper gas reactant distribution is regarded as an important issue to achieve full potential as well as a long lifetime of fuel cells.

Reactant flow distribution in gas flow channels is complicated due to several factors including the presence of the porous GDL. Since the pressure gradient caused by the GDL results in fluid leakage across the flow channels, gas flow rate was found to be different from the inlet to the outlet of individual channels and vary between parallel channels [3]. The reactant flow rate in the inlet of an individual channel can be employed as a measure of gas-liquid two phase flow distribution in parallel channels. Kandlikar et al. [39] introduced a technique to investigate gas-liquid flow mal-distribution through individual channels called the entrance region pressure drop measurement technique. Through both in situ and ex situ experiments, they found that using a porous GDL backing resulted in a non-uniform flow distribution in comparison with using an impermeable backing under similar operating conditions. Their results were further validated by high-speed images of the fluid flow mal-distribution along the parallel channels.

In general, two-phase flow mal-distribution in parallel mini-channels is related to the presence of a negative slope of pressure drop against superficial gas velocity in the gas–liquid mixture flow. Zhang et al. [40] investigated the direct effect of changing gas flow rate on two phase flow distribution in PEMFC parallel channels. They indicated that at low superficial gas velocity, flow mal-distribution corresponding to slug flow patterns was more likely to occur. Therefore, sufficiently high gas velocities are required to avoid reactant mal-distribution in parallel channels.

In addition, flow hysteresis phenomena were observed when starting from either flooded or dry conditions. Starting with stagnant flow conditions with gas introduced into channels flooded with water, both gas and liquid tended to flow preferentially in one of the channels leading to a flow mal-distribution at low superficial gas or liquid velocities. With increasing the superficial gas velocity, uniform reactant flow distribution in both gas channels could be detected with a sudden decrease in the pressure drop. Any further increase in the gas velocity led to a transition from slug flow to stratified flow in both channels. In contrast, when liquid water was introduced into initially dry-gas channels, even two-phase flow distribution in both channels could be achieved at lower gas flow velocities compared to the case of initial flooded channels [40].

2.7 References

[1] A. Bazylak, Liquid water transport in fuel cell gas diffusion layers, PhD thesis, University of Victoria, (2008).

[2] S. Litster, C. R. Buie, T. Fabian, J. K. Eaton, and J. G. Santiago, Active Water Management for PEM Fuel Cells, J. Electrochem. Soc. 154 (2007) B1049–B1058.

[3] R. Anderson, L. Zhang, Y. Ding, M. Blanco, X. Bi, and D. P. Wilkinson, A critical review of two-phase flow in gas flow channels of proton exchange membrane fuel cells, J. Power Sources. 195 (2010) 4531–4553.

[4] A. Bazylak, Liquid water visualization in PEM fuel cells: A review, Int. J. Hydrogen Energy. 34 (2009) 3845–3857.

[5] T. A. Trabold, J. P. Owejan, D. L. Jacobson, M. Arif, and P. R. Huffman, In situ investigation of water transport in an operating PEM fuel cell using neutron radiography: Part 1 - Experimental method and serpentine flow field results, Int. J. Heat Mass Transf. 49 (2006) 4712–4720.

[6] C. M. Lewandowski, Two-Phase Flow in Microchannels with Application to PEM Fuel Cells, PhD thesis, University of Victoria, (2015).

[7] A. Bazylak, D. Sinton, and N. Djilali, Dynamic water transport and droplet emergence in PEMFC gas diffusion layers, J. Power Sources. 176 (2008) 240–246.

[8] X. G. Yang, F. Y. Zhang, A. L. Lubawy, and C. Y. Wang, Visualization of Liquid Water Transport in a PEFC, Electrochem. Solid-State Lett. 7 (2004) 408–A411.

[9] K. S. Chen, M. A. Hickner, and D. R. Noble, Simplified models for predicting the onset of liquid water droplet instability at the gas diffusion layer/gas flow channel interface, Int. J. Energy Res. 29 (2005) 113–1132.

[10] C. Hidrovo, Hidrovo, F. Wang, J. Steinbrenner, E. Lee, S. Vigneron, Ch. Cheng, E. Hsiang, K. Goodson, Water slug detachment in two-phase hydrophobic microchannel flows, Proc. ICMM2005 3rd Int. Conf. Microchannels Minichannels, Toronto, Ontario, Canada, June 13-15, (2005) 1–7.

[11] M. Mortazavi and K. Tajiri, Effect of the PTFE content in the gas diffusion layer on water transport in polymer electrolyte fuel cells (PEFCs), J. Power Sources 245 (2014) 236–244.

[12] E. C. Kumbur, K. V. Sharp, and M. M. Mench, Liquid droplet behavior and instability in a polymer electrolyte fuel cell flow channel, J. Power Sources. 161 (2006) 333–345.

[13] P. Rahimian, R. Anderson, L. Zhang, Predictions of Flow Regimes in Proton Exchange Membrane Fuel Cells: An Analytical Approach. Int. J. Hydrogen Energy. 42 (2017) 4679–4689.

[14] F. Y. Zhang, X. G. Yang, and C. Y. Wang, Liquid water removal from a polymer electrolyte fuel cell, J. Electrochem. Soc. 153 (2006) A22.5

[15] B. Carroll and C. Hidrovo, Droplet detachment mechanism in a high-speed gaseous microflow, J. Fluids Eng.135 (2013) 071206-1, 071206-8.

[16] S. Chan, Y. Wang, and K. S. Chen, Droplet dynamics in a polymer electrolyte fuel cell gas flow channel : Forces, Deformation and detachment. II : Comparisons of analytical solution with numerical and experimental results, J. Power Sources. 210 (2012) 191–197.

[17] A. Theodorakakos, T. Ous, M. Gavaises, J. M. Nouri, N. Nikolopoulos, and H. Yanagihara, Dynamics of water droplets detached from porous surfaces of relevance to PEM fuel cells, J. Colloid Interface Sci. 300 (2006) 673–687.

[18] P. Pei, Y. Li, H. Xu, and Z. Wu, A review on water fault diagnosis of PEMFC associated with the pressure drop, Appl. Energy. 173 (2016) 366–385.

[19] R. Anderson, E. Eggleton, and L. Zhang, Development of two-phase flow regime specific pressure drop models for proton exchange membrane fuel cells, Int. J. Hydrogen Energy. 40 (2014) 1173–1185.

[20] I. S. Hussaini and C. Y. Wang, Visualization and quantification of cathode channel flooding in PEM fuel cells, J. Power Sources. 187 (2009) 444–451.

[21] C. E. Colosqui, M. J. Cheah, I. G. Kevrekidis, and J. B. Benziger, Droplet and slug formation in polymer electrolyte membrane fuel cell flow channels: The role of interfacial forces, J. Power Sources. 196 (2011) 10057–10068.

[22] A. Günther, S. A. Khan, M. Thalmann, F. Trachsel, and K. F. Jensen, Transport and reaction in microscale segmented gas–liquid flow, Lab Chip. 4 (2004) 278–286.

[23] T. C. Wu and N. Djilali, Experimental investigation of water droplet emergence in a model polymer electrolyte membrane fuel cell microchannel, J. Power Sources. 208 (2012) 248–256.

[24] M. M. Daino and S. G. Kandlikar, Evaluation of Imaging Techniques Applied to Water Management Research in PEMFCs, ASME 2009 7th International Conference on Nanochannels, Microchannels, and Minichannels. ASME Conf. Proc. Pohang, South Korea, June 22–24 (2009) 467–479.

[25] S. Tsushima, K. Teranishi, K. Nishida, and S. Hirai, Water content distribution in a polymer electrolyte membrane for advanced fuel cell system with liquid water supply, Magn. Reson. Imaging.23 (2005) 255–258.

[26] K. W. Feindel, S. H. Bergens, and R. E. Wasylishen, Use of hydrogen-deuterium exchange for contrast in ^{1}H NMR microscopy investigations of an operating PEM fuel cell, J. Power Sources 173 (2007) 86–95.

[27] K. W. Feindel, S. H. Bergens, and R. E. Wasylishen. The influence of membrane electrode assembly water content on the performance of a polymer electrolyte membrane fuel cell as investigated by 1H NMR microscopy, Phys. Chem. Chem. Phys. 9 (2005) 1850–1857.

[28] D. Spernjak, A. K. Prasad, and S. G. Advani, Experimental investigation of liquid water formation and transport in a transparent single-serpentine PEM fuel cell, J. Power Sources. 170 (2007) 334–344.

[29] N. Pekula et al., Study of water distribution and transport in a polymer electrolyte fuel cell using neutron imaging, Nucl. Instruments Methods Phys. Res. 542 (2005) 134–141.

[30] J. Zhang, J. Kramer, D. Shimoi, R. Ono, Y. Lehmann, E. Wokaun, A. Shinohara, K. Scherer, G. Günther, In situ diagnostic of two-phase flow phenomena in polymer electrolyte fuel cells by neutron imaging: Part B. Material variations, Electrochim. Acta. 51 (2006) 2715–2727.

[31] A. Turhan, K. Heller, J. S. Brenizer, and M. M. Mench, Passive control of liquid water storage and distribution in a PEFC through flow-field design, J. Power Sources. 180 (2008) 773–783.

[32] I. Manke, C. Hartnig, M. Grunerbel, W. Lehnert, N. Kardjilov, A. Haibel, A. Hilger, J. Banhart, H. Riesemeier, Investigation of water evolution and transport in fuel cells with high resolution synchrotron x-ray radiography, Appl. Phys. Lett. 90 (2007) 174105.

[33] C. Hartnig, I. Manke, R. Kuhn, N. Kardjilov, J. Banhart, and W. Lehnert, Cross-sectional insight in the water evolution and transport in polymer electrolyte fuel cells. Appl. Phys. Lett. 92 (2008) 90–93.

[34] J. Lee, J. Hinebaugh, and A. Bazylak, Synchrotron X-ray radiographic investigations of liquid water transport behavior in a PEMFC with MPL-coated GDLs, J. Power Sources. 227 (2013) 123–130.

[35] T. Sasabe, P. Deevanhxay, S. Tsushima, and S. Hirai, Investigation on the effect of microstructure of proton exchange membrane fuel cell porous layers on liquid water behavior by soft X-ray radiography, J. Power Sources. 196 (2011) 8197–8206.

[36] W. S. He, G. Y. Lin, and T. Van Nguyen, Diagnostic tool to detect electrode flooding in proton-exchange-membrane fuel cells, AIChE J. 49 (2003) 3221–3228.

[37] X. Liu, H. Guo, F. Ye, and C. F. Ma, Water flooding and pressure drop characteristics in flow channels of proton exchange membrane fuel cells, Electrochim. Acta. 52 (2007) 3607–3614.

[38] E. See and E. J. See, In situ measurement, characterization, and modeling of two-phase pressure drop incorporating local water saturation in PEMFC gas channels In Situ Measurement, Characterization, and Modeling of Two-Phase Pressure Drop Incorporating Local Water Saturation, M.Sc. thesis, Rochester Institute of Technology (2013).

[39] R. Banerjee, D. Howe, V. Mejia, and S. G. Kandlikar, Experimental validation of two-phase pressure drop multiplier as a diagnostic tool for characterizing PEM fuel cell performance, Int. J. Hydrogen Energy. 39 (2014)17791–17801.

[40] S. G. Kandlikar, Z. Lu, W. E. Domigan, A. D. White, and M. W. Benedict, Measurement of flow mal-distribution in parallel channels and its application to ex-situ and in-situ experiments in PEMFC water management studies, Int. J. Heat Mass Transf. 52 (2009) 1741–1752.

[41] L. Zhang, H. T. Bi, D. P. Wilkinson, J. Stumper, and H. Wang, Gas-liquid two-phase flow patterns in parallel channels for fuel cells, J. Power Sources. 183 (2008) 643–650.

Chapter 3 - Predictions of flow regimes in proton exchange membrane fuel cells: an analytical approach

The contents of this chapter have been published in the International Journal of Hydrogen Energy (Rahimian P., Anderson R., Zhang, L.F., International Journal of Hydrogen Energy, 2017, 42(7), 4679-4689.).

Contribution of the MSc student

The analytical approach was proposed by Lifeng Zhang. Calculations and data analysis were performed by Paria Rahimian. Paria Rahimian and Lifeng Zhang prepared the manuscript with Ryan Anderson providing technical and editorial guidance throughout preparation. Lifeng Zhang supervised and provided consultation during thesis preparation.

Contribution of this chapter to the overall study

In this Chapter, the stability of growing water droplets was determined under different operating conditions relevant to a fuel cell. Also, an analytical approach was proposed to predict which flow pattern was likely to occur after droplet detachment. Analysis of the Damkohler number was performed in a range of superficial gas and liquid velocities of importance to PEMFCs. In addition, a force balance analysis was utilized to determine the critical detachment diameter of droplets. Using critical detachment diameters as an input, the forces required to remove different flow patterns were calculated.

3.1 Abstract

Water management in proton exchange membrane (PEM) fuel cells still remains a topic of much investigation in order to maintain satisfactory cell performance. One specific water management issue relates to the gas-liquid flows that occur when water enters the reactant flow field channels, which are typically micro-channels or mini-channels. The emergence of liquid water in the flow channel is very unique, starting with a form of liquid droplet. The liquid droplet grows and becomes unstable at high gas velocities. Detachment of unstable droplets leads to various flow regimes possibly observed in active fuel cells, including droplet, slug, film, and mist flows. In this work, a force balance analysis was conducted to determine the stability of a liquid droplet under different operating conditions of relevance to fuel cell operation. After droplet detachment, a theoretical approach was developed to define which flow regime will form. The force balance analysis considered different wetting scenarios in the channels and a range of superficial velocities of importance to PEM fuel cells was taken into account.

3.2 Introduction

Proton exchange membrane (PEM) fuel cells electrochemically convert oxygen and hydrogen into electricity, water, and heat. They represent a potential clean energy technology with high power density, no emissions (e.g. CO_2, NOx) during use, and the ability to run continuously while reactants are supplied. Properly managing the water produced by the electrochemical reaction is critical to high performance and durable operation [1-3]. A complex water balance exists throughout the cell, and the influence of water must be considered in each layer of the fuel cell (membrane, catalyst layers, porous gas diffusion layers, and flow field channels) [3]. At the extremes of water management are cases of ‘flooding’ and ‘drying’. Too much water ‘floods’ cell

components, which impedes the gas from reaching the active catalyst sites. Insufficient water dehydrates the membrane, substantially reducing proton conductivity. In addition to a drop in performance via a reduction in voltage, water accumulation in the flow channel leads to a less stable voltage signal [4, 5] and increases the pressure drop in the channels [6-8], which is a parasitic power loss [9]. Thus, the fuel cells typically operate in a narrow range for optimal hydration and performance.

While water management is an issue in all of the fuel cell components, gas-liquid two-phase flow in the flow field channels has received specific attention [10]. In the literature, experimental studies of the multiphase flow in fuel cell channels have been performed via in-situ (electrochemically active) and ex-situ experimental set-ups. Experimental and numerical studies have focused on two-phase flow patterns and on droplet dynamics in PEM fuel cells. The key flow patterns in PEM fuel cells are [11-12]:

(1) Single phase flow: in this flow regime, hardly any water droplets can be observed on the GDL surface and the flow is mostly in the form of partially humidified gas.

(2) Droplet flow: this flow regime is dominated by water droplets that emerge from underneath the GDL surface and remain adhered to the surface by surface tension forces.

(3) Film flow: film flow occurs at high water influx through the GDL. Droplet coalescence forms a liquid film of growing thickness.

(4) Slug flow: further growth of the film causes it to accumulate into a slow-moving slug. This causes oscillations in pressure and voltage signals.

(5) Accumulation: slugs, droplets, and films occur with insufficient air flow to remove the liquid and/or insufficient time for droplets to grow to the critical size.

This two-phase flow starts with emergence of liquid droplets, which emerge from the porous gas diffusion layer perpendicular to the direction of gas flow. Afterwards, liquid droplets are subject to shear forces from the gas stream during the droplet growth. Therefore, a detailed understanding of liquid droplet dynamics is necessary to determine the subsequent flow patterns formed. Studies have examined droplet dynamics through numerical simulations and experiments. In micro-channels, the surface tension, inertia, and viscosity are important parameters. With respect to experimental efforts, typical non-reactive fuel cells or microfluidic devices are employed to elucidate mechanisms of droplet growth and removal. Table 2.1 summaries the main research works on liquid droplet dynamics since 2010. Wu and Djilali [13] used a microfluidic platform to investigate water droplet emergence in a cathode side flow channel of a PEM fuel cell. Three distinct flow regimes were identified: slug flow, droplet flow, and film flow under different gas and liquid flow rates. Slug flow occurs at low gas superficial velocities. Droplet flow was observed at increasing air velocity with an individual droplet emerging from the water pore, and it remained pinned at the water pore due to surface tension forces until it grew to a critical size. Colosqui et al. [14] also employed a microfluidic device to investigate flow patterns related to fuel cell operation. It is found that the geometry of the flow channel and interfacial forces were dominating factors in determining the size of slugs and the work required to remove liquid slugs. In two related works by Cheah et al. [15, 16], the effect of wall wettability on flow patterns was investigated. It has been found that slugs formed in hydrophobic channels are smaller than those formed in hydrophilic channels.

Table 3.1 Summary of publications on liquid droplet dynamics and flow regime predictions relevant to fuel cell operation (since 2010).

Reference	Microfluidic Device	Operating Conditions	Findings
Wu and Djilali [13]	PDMS chip; Channel cross section: 250 μm X 250 μm a single square pore: 50 μm X 50 μm Channel length: 37 mm	Air flow rate (sccm): 12-300 Air superficial gas velocity 9 m/s): 3.2 - 80 Water flow rate (mL min^{-1}): 3, 6, 15 Water superficial velocity (m/s): 0.02, 0.04, 0.010	Three distinct flow regimes were observed: slug flow, droplet flow, and film flow.
Esposito et al. [17]	Plexiglas plate; Channel cross section: 13 mm X 13 mm; Channel length: 0.5 m; Toray paper 120: 5%, 10%, and 20% PTFE	Air superficial gas velocity: 14.5 m/s to 25.3 m/s	The droplet size decreased with increasing air velocity. The droplet oscillation frequency did not depend upon air velocity but was influenced by droplet size.
Colosqui et al. [14]	Acrylic plates: 1.6 mmX1.6 mm; Channel length: 125mm A single square micropore: 50 X 50 μm	Gas flow rate: 3-21 ml min^{-1}; Liquid flow rate:5-75 μL/min (The flow rates were based on a maximum current density of 1.3 A cm-2 for a 10 cm2 active area fuel cell)	The geometry of the flow channel and interfacial forces were dominant factors deterring the size of slugs and the work required to remove liquid water.
Cho et al. [18]	Chanel cross section: 1.6 mm X 1.0 mm; GDL: Toray carbon paper with 30% PTFE loading	Air flow velocity: 0-8.75 m/s;	Droplet deformation and detachment velocity were qualitatively comparable to experimental data.

Cheah et al. [15,16]	Channel materials: uncoated acrylic and coated acrylic; Cross section area: 1.6 mm X 1.6 mm (Square); 2.4 mm X 1.1 mm (rectangular); 1.6 mm (semi-circular)	Nitrogen gas flow rates: 3-21 ml/min; Water flow rates: 5-50 ml/min;	Slugs formed in hydrophobic channels and semi-cylindrical channels are smaller than slugs formed in hydrophilic square or rectangular channels. Hydrophilic channel produced large slugs that would minimize the energy of water removal.
Hellstern et al. [19]	Channel material: acrylic plate for three walls; GDL: Toray carbon paper (TGP-H-120) with 20%; Two square channels: 1.6 mm X 1.6 mm X 125mm; A single pore: 100 μm	Nitrogen flow rate: 2-18 mL/min ($Re_G < 20$); Water flow rate: 10-75 μL/min	Water slug forms at low gas flow rates in hydrophobic channels; gas bypass beneath the ribs from one flow channel to the adjacent channel slowed down slug motion and slug became stationary; the volume of slugs, the velocity of slug motion and the pressure required to remove slugs can be determined by force balance.
Ye et al. [20]	Two parallel channels: 1.6 mm X 1.6 mm X 125 mm; Acrylic plate; Pore size: 100 mm	Nitrogen flow rate: ~ 100 ml/min ($Re_G < 36$); Water flow rate: 10 μL/min;	Gas flow can bypass slugs blocking the channel by flow through the GDL; slugs detach and move when the pressure drop for gas to flow beneath the GDL under the slug is equal to the detachment pressure of the slug.

The bubbly flow pattern is not typically observed in PEM fuel cells due to the required high ratios of liquid flow rates to gas flow rates. While not directly related to the conditions experienced in a PEM fuel cell, these works provide a strong framework for extension to PEM fuel cells.

As real fuel cell materials (e.g. graphite bi-polar plates) are typically opaque, advanced visualization tools have been used to see dynamic water flow behaviors in fuel cell flow channels. Experiments that observe the gas-liquid flow in the flow field channels are reviewed in [10], and similar in situ systems that provide the experimental data for this paper are in [11,21,22]. Advances in visualization (e.g. X-ray radiography, MRI) have led to a better understanding of how liquid water transports through various layers in the cell.

Hussaini and Wang presented the first major in situ effort toward a flow regime map [11]. Their work showed that at moderate to high gas flow rates, water can be removed as a mist. Droplets coalesced towards the outlet of the fuel cell and/or at the bends of serpentine flow channels. After coalescing, droplet flow changed into film/annular flow or slug flow. Film flow typically occurs at the corner of the gas flow channels and transitioned to slug flow if the film grows to a critical thickness. These patterns are shown in Figure 3.1a.

In addition to the above defined flow patterns [11], Anderson et al. [12] introduced a new flow regime, the accumulating flow regime, based on pressure drop data collected from active fuel cells. The ‘accumulating’ flow regime occurs if the liquid residence time is so large that the liquid is effectively stagnant. That analysis was done on the basis of high pressure drops that were inconsistent with pressure drop predictions of the other regimes. Long residence times of slugs were noted in an ex situ setup [28] and via MRI [29]. The boundaries for the accumulating regime [12] and regimes from Hussaini and Wang [11] are shown in Figure 3.1b.

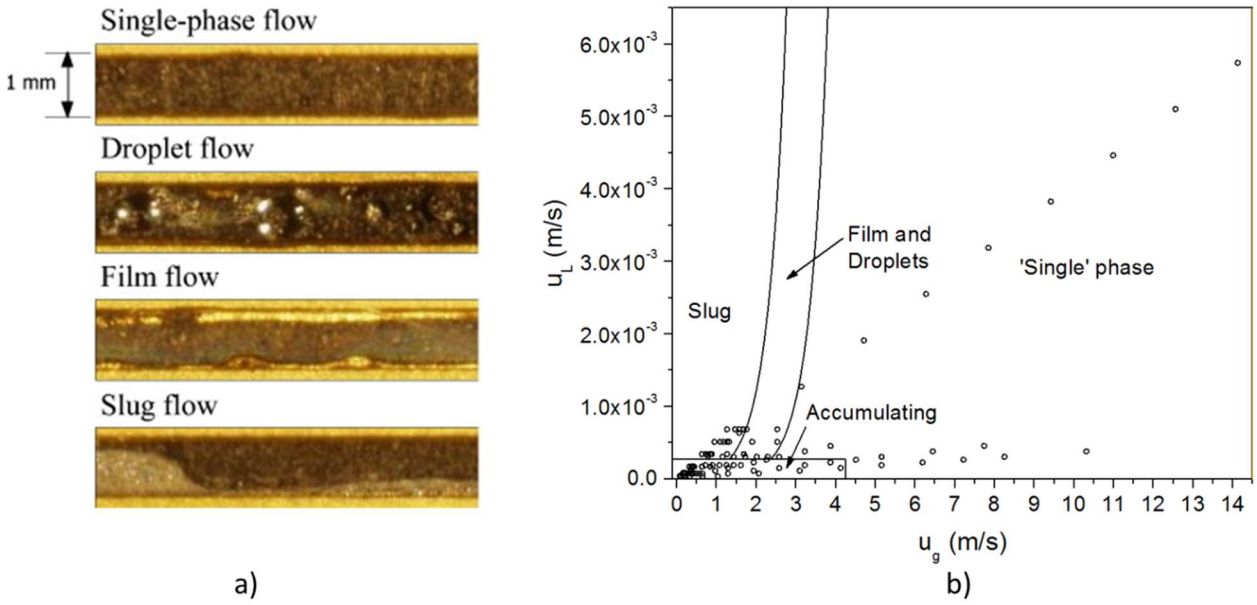

Figure 3.1 a) Flow pattern images from Hussaini and Wang [11]. B) Flow regime map from Anderson et al. [12] showing the approximate regions of the slug, film, single-phase, and accumulating flow regimes. Here, u_g represents superficial gas velocity and u_L represents superficial liquid velocity. [With permission from Elsevier].

The experimental efforts are complemented by computational fluid dynamics (CFD) studies for detailed analysis [30-36]. While a powerful tool, CFD techniques can be computationally intensive when considering relevant spatial and temporal scales of an active fuel cell.

It has been noted that the pressure drop is a function of flow regime and the flow regime specific pressure drop model requires a clearly defined flow regime map [12]. Therefore, there is a prerequisite to know what flow pattern forms under a particulate set of operating conditions before predicting two-phase flow pressure drop. In addition, onset of two-phase flow should be determined. Wang and Chen [37] first attempted to distinguish single-phase flow from two-phase flow with a dimensionless group, the Damkohler number (Da_0), defined below:

$$Da_0 = \frac{\text{Rate of Water Production}}{\text{Rate of water removal via vapor diffusion}} \tag{3.1}$$

Based on the above equation, the following statements were made [37]:

1) When $Da_0 \rightarrow 0$, single-phase flow is expected.
2) In contrast, two-phase flow will be encountered when $Da_0 \rightarrow \infty$. The Damkohler number proposed only distinguished the single-phase flow regime from two-phase flow regimes.
3) When $Da_0 = 0(1)$, liquid water might be observed in some parts of the fuel cell.

Wang and Chen [37] used this dimensionless number to illustrate possible two-phase flows across the channel. However, this number does not provide further information with respect to what kind of flow pattern forms.

Though a few studies have been reported on droplet dynamics, there is no clear picture of how droplet instability leads to different flow patterns after liquid droplet detachment from the GDL surface. Therefore, the objectives of this work were to present a theoretical approach to predict two-phase flow patterns under active fuel cell operation conditions. A force balance was made on liquid droplets. After liquid droplets detach, based on their critical droplet sizes, the resultant pressure forces were calculated and compared to forces required for different flow pattern, and a flow pattern was determined. These predictions are compared to the flow pattern maps in [11,12]. A sensitivity analysis is conducted to show the effects of contact angle and contact angle hysteresis.

3.2.1 Force balance around a droplet

A review of water droplet detachment is provided by Schillberg and Kandlikar [38]. Water emerging into the channels from the porous gas diffusion layer can appear in preferential areas [39-41]. However, those locations can vary temporally [42] and spatially (including whether or not the liquid touches the landing areas) [43]. The focus of the gas-liquid flow is typically on the cathode side where the water is produced. Droplet behavior depends on the air flow rate, water

injection rate, and material contact angles [40]. Gas diffusion layers are typically PTFE treated to make the layers hydrophobic (contact angles greater than 90°), but the advancing and receding contact angles that appear as the droplet deforms due to air flow must also be considered [44-46].

We followed the methods proposed by Chen et al. [47] and Cho et al. [48] to predict the critical droplet size in the gas flow channel [49]. While the full details are available in those references, a brief summation is provided again here for clarity. The method emerges from a force balance over a droplet in the channel as shown in Figure 3.2.

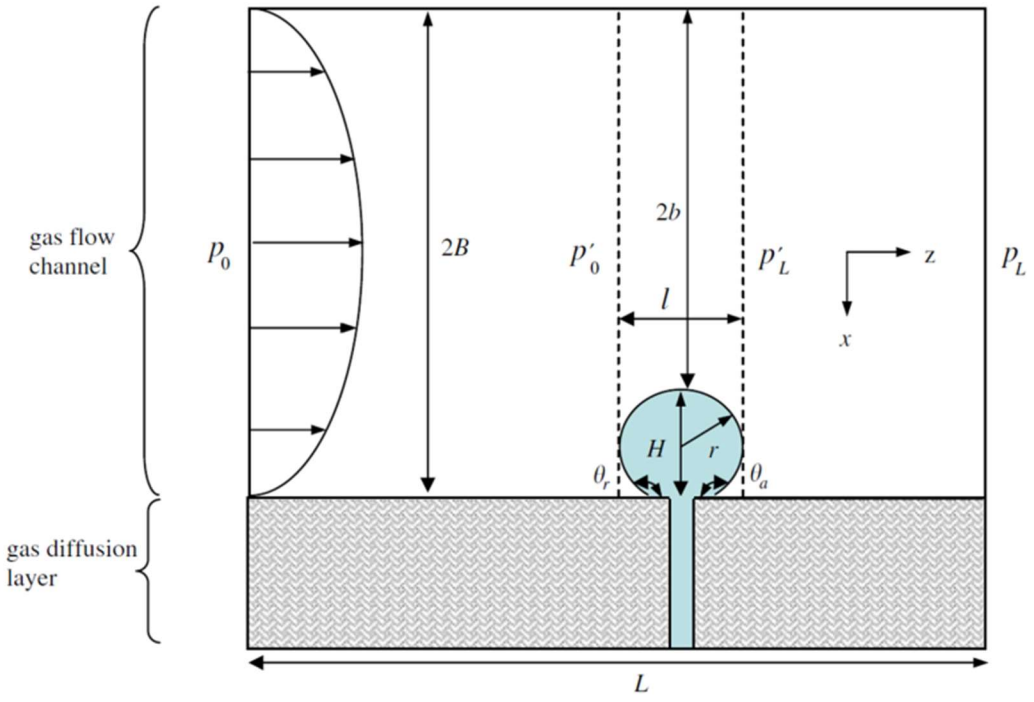

Figure 3.2 Schematic of a liquid droplet in a flow channel [47] (with permission from Wiley Inter Science).

The macroscopic force balance along the channel flow direction within the control volume gives:

$$(p_0^{'} - p_L^{'})2Bl + l^2\tau_{xz}^{w} + f_{\mu,d} = 0\,. \tag{3.2}$$

Here, $p_0^{'}$ and $p_L^{'}$ are the gas pressure immediately upstream and downstream of the droplet, p_0 and p_L are the gas pressure upstream and downstream of the gas flow channel. $2B$ is the channel height,

H is the droplet height, r is the droplet diameter, L is the channel length and l is the distance of the upstream and downstream surfaces. The second term in the left-hand side in Equation (2) is the shear stress exerted by the flowing gas on the top wall in an area of l, which is the projected area of the droplet. The term $f_{\mu,d}$ is the viscous drag force exerted on the droplet by the flowing gas. The analysis assumes fully developed laminar Newtonian gas flow [47-48]. Cho et al. [18] derived a relationship between the detachment velocity and the droplet size based on the drag coefficient estimation;

$$We_r = \left[\frac{4}{a_{Cho}} \frac{\pi \sin^2 \theta_s \sin(1/2)(\theta_a - \theta_r)}{(\theta_s - \sin\theta_s \cos\theta_s)} \right] \mathrm{Re}_g^{-b_{Cho}} \quad , \tag{3.3}$$

Where θ_a is advancing contact angle, θ_r is receding contact angle, θ_s is the static contact angle and We_r is the Weber number, defined as the ratio between fluid inertia and surface tension:

$$We = \frac{\rho u_g{}^2 R_0}{\gamma}. \tag{3.4}$$

The Reynolds number with respect to the gas flow is given by

$$\mathrm{Re}_g = \frac{\rho u_g (2B)}{\mu}. \tag{3.5}$$

The constants a_{Cho} and b_{Cho} are estimated based on the following equations [18]:

$$a_{Cho} = 46.27 \times \left(\frac{D}{(2B)} \right)^{0.1757}; \tag{3.6}$$

$$b_{Cho} = 0.2158 \times \left(\frac{D}{(2B)} \right) - 0.6384. \tag{3.7}$$

Critical droplet sizes are predicted according to Equation (3) and the relationships in Equations (4)-(7) under a set of given operating conditions. The physical properties involved in the

calculation were corrected based on the actual operating conditions of each group (temperature, pressure, relative humidity, channel design, gas stoichiometry, and current density).

3.2.2 Flow regime assignment

Most of previous studies on droplet dynamics did not reveal the final fate of a detached droplet. This work provides qualitative analysis of flow patterns formed in active fuel cells. Once the critical droplet size reaches the channel diameter, the droplet is considered to be unstable and detaches from the GDL surface. Forces required to move liquid water in flow channels vary with different flow patterns. The force needed to move the partial liquid bridge is equal to the force needed to move the gas-liquid-solid contact lines in the direction of the gas flow, given by Cheah et al. [15]:

$$F_{drop\ motion} = (2h + w)\gamma_{adv} - (2h + w)\gamma_{rec} = (2h + w)\gamma_w(\cos\theta_{A,dyn} - \cos\theta_{R,dyn}) \quad . \tag{3.8}$$

Here, h represents critical droplet diameter, w represents channel width, γ_{adv} represents advancing surface tension, γ_{rec} represents receding surface tension. When the drop spans the channel and forms a slug, the force for slug motion is given by;

$$F_{slug\ \ motion} = 4w\gamma_w(\cos\theta_{A,dyn} - \cos\theta_{R,dyn}) \quad . \tag{3.9}$$

When the liquid droplet reaches a critical size, it will detach from the GDL surface and then will be purged out of the flow channel. The procedure and flow pattern assignment is depicted in Figure 3.3.

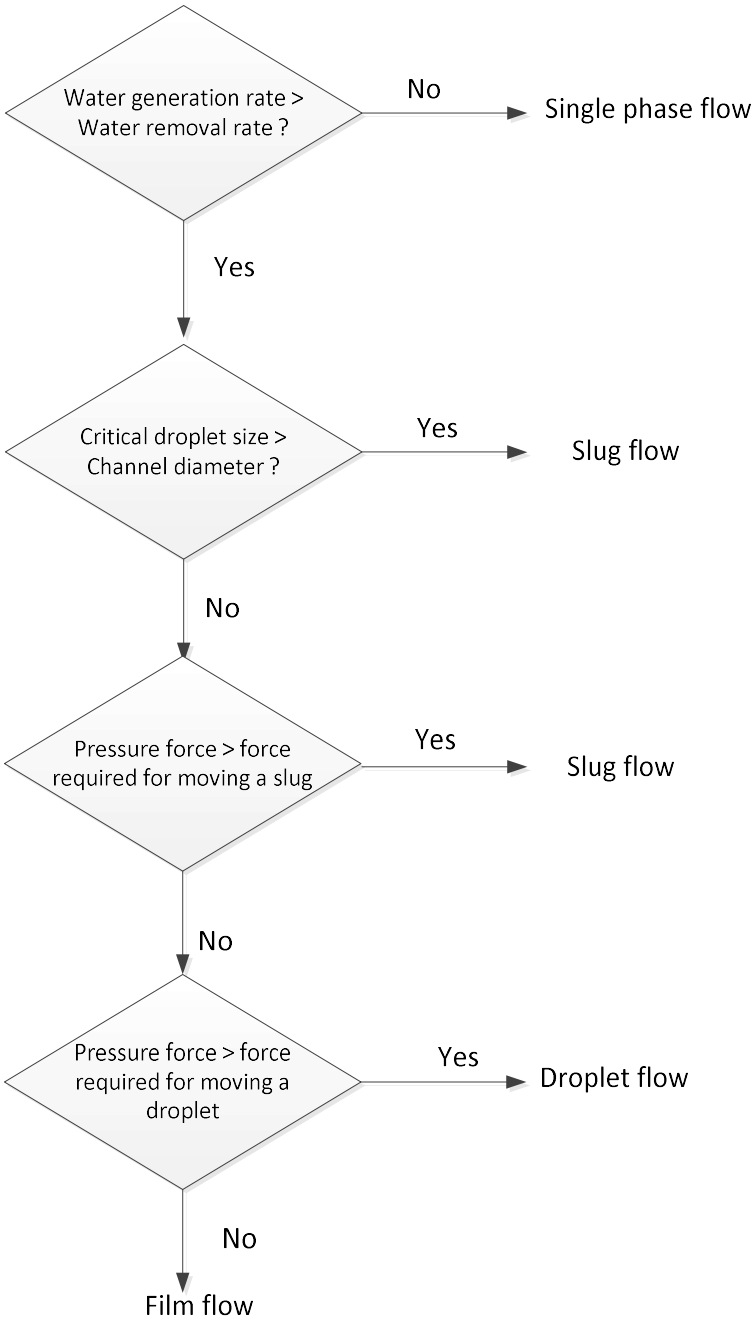

Figure 3.3 Flow regime assignment algorithm to determine slug, droplet, and film flow.

The detailed procedure is explained as follows:

(1) Critical droplet sizes are calculated according to Equation (8) based on channel geometries of active fuel cells and operating conditions;

(2) Compare to channel sizes from active fuel cell data;

(3) Slugs will be formed once the critical droplet size reaches the height of the flow channel;

(4) Using the resultant critical droplet sizes to calculate pressure forces exerted by the gas flow, compare with that required for droplet and slug motions. If the pressure force is larger than that needed for slug motion, then droplets will form slugs after detachment. Otherwise, droplet flow is assigned.

(5) If the pressure force is smaller than that for droplet motion, a film flow likely occurs.

3.3 Results and discussion

Before developing a method to predict a two-phase flow pattern, it is essential to confirm the on-set of two-phase flows in the available in-situ data [11, 21, 22]. Based on evaluations of the Damkohler number proposed by Wang and Chen [37], Figure 3.4 shows an example of how Da_0 varies with air relative humidity and current density. The resistance in the gas diffusion layer is estimated by H_{GDL}/D^{eff}_{dry} [50]. H_{GDL} represents GDL thickness and D^{eff}_{dry} represents effective diffusivity of a dry gas diffusion layer. With an increase in current density (assuming as 25 cm^2 cell), Da_0 increases as the liquid water production rate is a direct function of the current via Faraday's Law. Thus, liquid water is more likely to appear. Da_0 also increases substantially with RH as the rate of water removal via diffusion decreases. For example, when RH = 90%, the two-phase flow will occur for a wide range of operating conditions. Even at a low relative humidity such as RH = 25%, $Da_0 =$ 0(1), so two-phase flows likely occur in both the GDL and the gas flow channel. The effective diffusivity is also influenced by the liquid saturation, meaning Da_0 could larger than the values shown in Figure 3.4.

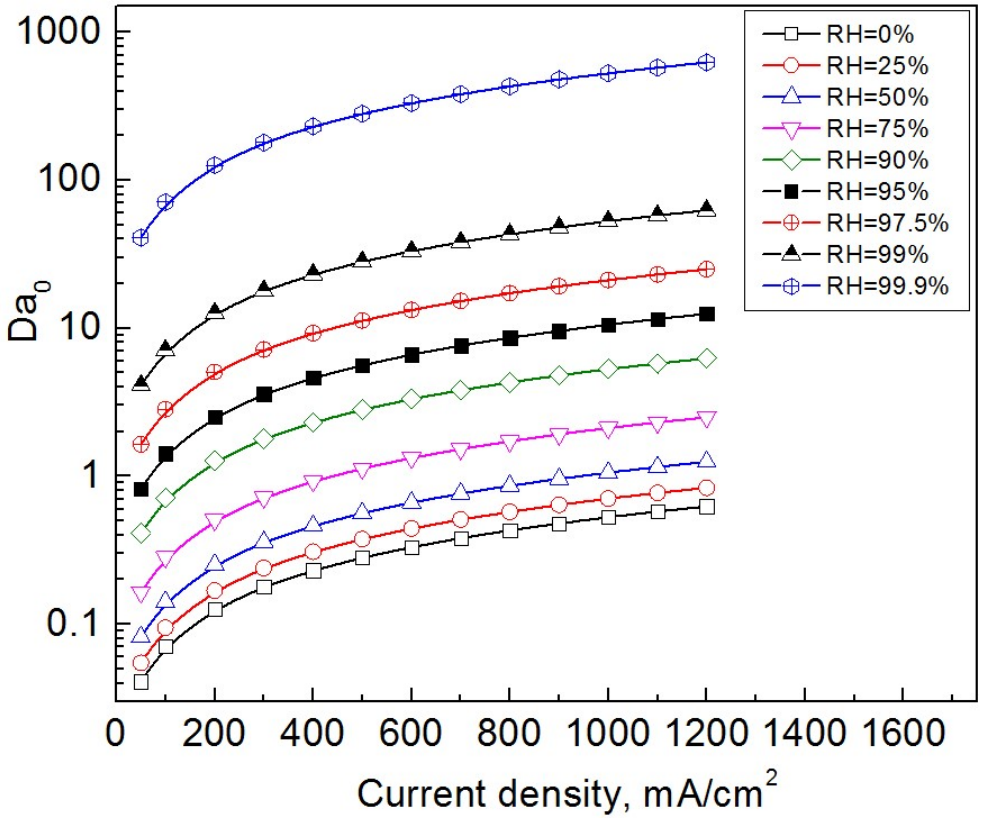

Figure 3.4 Predicted Da0 number under different relative humidity conditions over a range of current densities.

The range of Da0 numbers for three active fuel cells [11, 21, 22] was evaluated and the range of results are shown in the Table *3.2*. The discrete data points correspond to actual experimental conditions from the three fuel cells.

Table 3.2 Range of Da0 number for active fuel cells from See [22], Hussaini and Wang [11], and Anderson et al. [21].

Group	Conditions for min Da_0	Conditions for max Da_0	Range of Da_0
See [22]	Temperature: 60 °C Gas stoichiometry: 8 Humidity: 0% GDL thickness: 0.190 (mm) Current density: 50 (mA/cm^2)	Temperature: 40 °C Gas stoichiometry: 1.5 Humidity: 95% GDL thickness: 0.245 (mm) Current density: 1000 (mA/cm^2)	0.02 < Da < 26.9
Hussaini and Wang [11]	Temperature: 80 °C Gas stoichiometry: 4 Humidity: 26% GDL thickness: 0.230 (mm) Current density: 200 (mA/cm^2)	Temperature: 80 °C Gas stoichiometry: 2 Humidity: 66% GDL thickness: 0.230 (mm) Current density: 800 (mA/cm^2)	0.29 < Da < 2.4
Anderson et al. [21]	Temperature: 90 °C Gas stoichiometry: 4 Humidity: 100% GDL thickness: 0.190 (mm) Current density: 50 (mA/cm^2)	Temperature: 50 °C Gas stoichiometry: 1.5 Humidity: 100% GDL thickness: 0.235 (mm) Current density: 1000 (mA/cm^2)	16. 8 < Da < 1541

The Da0 number for the active fuel cell from See [22] is typically lower than the other sets. At the current density of 50 mA/cm^2 and dry conditions, Da_0 is low and on the order of 0(0.1), implying that single-phase flow is likely to be observed. However, at higher current densities and more humid gas conditions, two-phase flow is expected. Da_0 ranges from ~0.29 to 2.4 according to Hussaini and Wang's data [11], indicating that both single-phase flow and two-phase flow could be observed. It is clear that Da_0 is generally higher in the active fuel cell from Anderson et al. [21], indicating two-phase flow is inevitable in all cases. The high Da_0 in that data are attributed to a

fully saturated air stream, making water removal in the air stream minimal. To avoid Da_0 going to infinity at 100% RH, an RH of 99% was assigned to that estimate. As noted before, the Damkohler number alone is not adequate to determine which two-phase flow pattern emerges. However, this analysis does confirm two-phase flow is expected in many of the cases.

To remedy the shortcoming of the Da_0 analysis, a force balance analysis can be performed to determine whether the liquid droplet is stable. Based on the force balance analysis described in previous section, critical droplet diameters were predicted based on operating conditions in three active fuel cells [11, 21, 22]. The key parameters and conditions utilized to calculate the critical droplet sizes from the available experimental data are in Table 3.*3* [49].

Table 3.3 Conditions for the data collected here from [11, 21, 22] highlighting relevant parameters, including fuel cell design (active area, flow channel design) and cathode gas diffusion layer.

Variable	**Hussaini and Wang [11]**	**See and Kandlikar [22]**	**Anderson et al. [21]**
Active area (cm^2)	14	50	35.7
Flow-field	7 parallel channels	22 parallel channels	4 parallel channels
Range of air stoichiometries	2-4	2.5-8	1.5-4
Cathode GDLs	Toray carbon paper	MRC-105, Freudenberg H2315	SGL 25BC
Constant angle hysteresis (°)	5°	5°	5°
Channel dimensions *l*w*d* (mm)	100x1x0.5	273x0.7x0.4	300x1x1
GDL contact angle (°)	130	130	130

For all groups, the superficial gas velocity is determined from Faraday's Law, the gas stoichiometry, the channel design, and the operating conditions. Faraday's Law states that the amount of substance consumed in a fuel cell is directly proportional to the quantity of electricity produced. The gas stoichiometry defines the ratio of inlet reactant gas and reactant gas consumption inside the fuel cell. Detailed dimensions and operating conditions (temperature, pressure, relative humidity, gas stoichiometry) of these fuel cells are provided in [12].

From the resultant critical droplet sizes, two regions are defined for droplets: stable and unstable regions. In Figure 3.5a, a droplet below the calculated $D_{critical}$ line is stable while a drop above the line is unstable. Unstable droplets have reached the critical size and can detach from the GDL. The critical droplet size decreases as the superficial gas velocity increases, and this effect is much more pronounced at lower velocities (< 4 m/s). At higher gas velocities, the reduction in critical droplet size with superficial gas velocity is minor. This figure also shows the dependence of the critical droplet sizes on GDL contact angles and contact angle hysteresis. With an increase in the contact angle, the critical droplet size decreases at detachment. In contrast, the critical droplet size increases as the contact angle hysteresis increases. This result indicates that more hydrophobic surfaces produce smaller droplets, which is consistent with the current practice of PTFE treating the GDL surface to make it more hydrophobic.

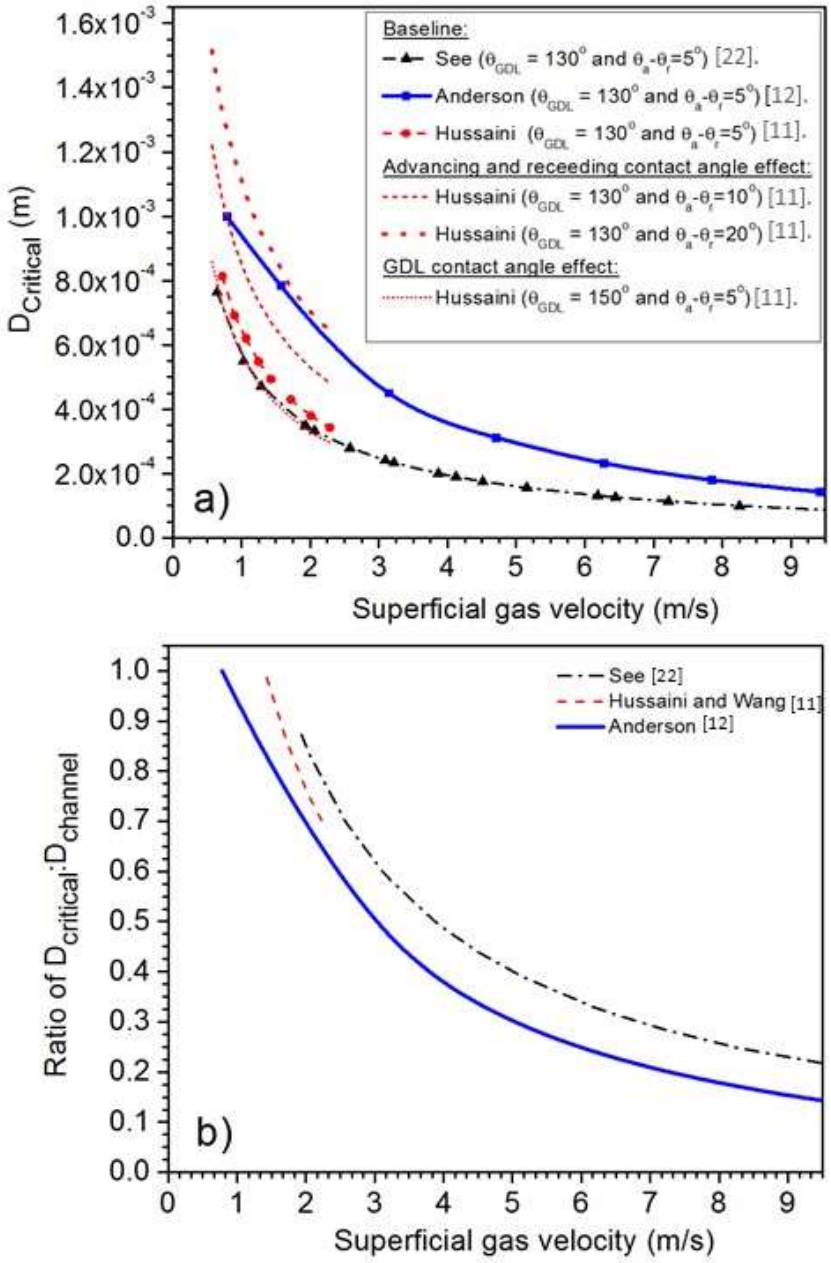

Figure 3.5 a) Comparison of normalized critical droplet sizes for three active fuel cells based on channel dimensions b) Critical droplet size examined as a function of contact angle hysteresis and GDL contact angle. Comparisons are made to data from Hussaini and Wang [11].

In this analysis, the critical droplet size is constrained by the diameter of the channel because it assumes the single droplet grows from the center of the GDL. Considering the force balance analysis is specific to a droplet centered on the gas diffusion layer, the analysis does not consider

the slug growing down the length of the channel while remaining stationary. If the droplet diameter reaches the channel diameter before reaching the critical detachment diameter, the droplet will wet the hydrophilic channel wall. That would cause detachment from the GDL independent of the force balance presented. Thus, the predicted critical droplet diameter was divided by the narrowest channel diameter to constrain this analysis. Figure 3.5b shows these results, and in general good qualitative agreement is noted between the groups. It is also important to note that the force analysis was only conducted on a single droplet in the flow channel. In actual fuel cells, multiple initial droplets can emerge along the flow channel. Once one droplet detaches from the GDL surface, it can combine with other downstream droplets, resulting in larger droplets. These effects are not considered here. However, the general approach is useful as the critical detachment diameter is used in the subsequent flow regime prediction algorithm from Figure 3.3.

The forces required for droplet motion, slug motion, and film motion are different as discussed by Cheah et al. [15]. Figure 3.6 shows typical pressure forces and forces required for droplet and slug motions based on See's data. The baseline values used in this analysis are a contact angle hysteresis of 10°, an advancing contact angle of 135°, and a receding contact angle of 125°. The advancing and receding contact angles are reasonable approximations for typical GDL materials [51].

It can be seen in Figure 3.6 that forces required for slug motion is always higher than droplet motion as expected. At slug motion, the whole cross-sectional area of the flow channel is obstructed, resulting in highest flow resistance. At low superficial gas velocities (corresponding to low current densities with typical stoichiometric ratios), the pressure forces are higher than forces required for both slug motion and droplet motion, indicating that slug flow is possible. When the superficial gas velocity is higher than 2 m/s in this data set, the available pressure forces is lower

than those required for both slug and droplet motion, indicating that either slug motion and droplet motion is unlikely to occur. Based on the flow regime assignment discussed earlier, film flow will form, at which the flow resistance is minimal.

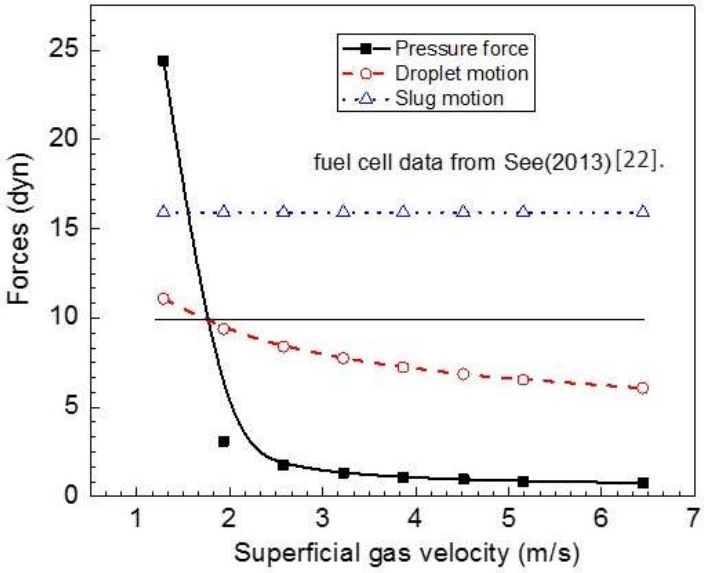

Figure 3.6 Pressure forces and forces required for different flow motions based on See's data [22].

Following the similar procedure, a flow regime assignment was conducted for the active fuel cell data. The resultant flow regime map is shown in Figure 3.7. The solid boundary lines represent flow regime boundary predictions from the empirical correlations developed by Hussaini and Wang [11] (also shown in Figure 3.1). In general, good qualitative agreement is noted between those empirical correlations and the new flow regime prediction presented here. In general, it can be seen that slug flow mainly is observed at the low superficial gas velocity and low superficial liquid velocity, corresponding to low current densities in active fuel cell operations. In the slug flow regime, two-phase flow multipliers are typically higher [12]. Film/droplet flow occurs at higher superficial gas velocities, corresponding to high current densities, which requires high gas flow rates at fixed gas stoichiometries. In this type of flow regime, flow resistance is lower than

that of slug flow. Therefore, two-phase multipliers are generally lower. Single-phase flow is observed at relatively high gas velocities.

Note that the flow regime map in Figure 3.7a does not include the accumulating regime as shown in Figure 3.1b. This is due to the dynamic injection of water into the flow field channel through the gas diffusion layer. The analysis in Figure 3.7 assumes droplets have already reached the critical diameter for detachment; the force calculations then predict which flow regime is likely to occur. However, at low current densities, the water production rate is quite low, meaning that it takes time for the droplets to reach a sufficient droplet size for removal. Figure 3.7b shows these results with the accumulating regime boundaries. The accumulating regime indicates an area where under typical testing conditions an insufficient amount of water is breaking through the GDL to form large enough droplets. Thus, the small droplets do not grow to the critical droplet size for detachment and adhere to the surface, causing higher than expected pressure drops.

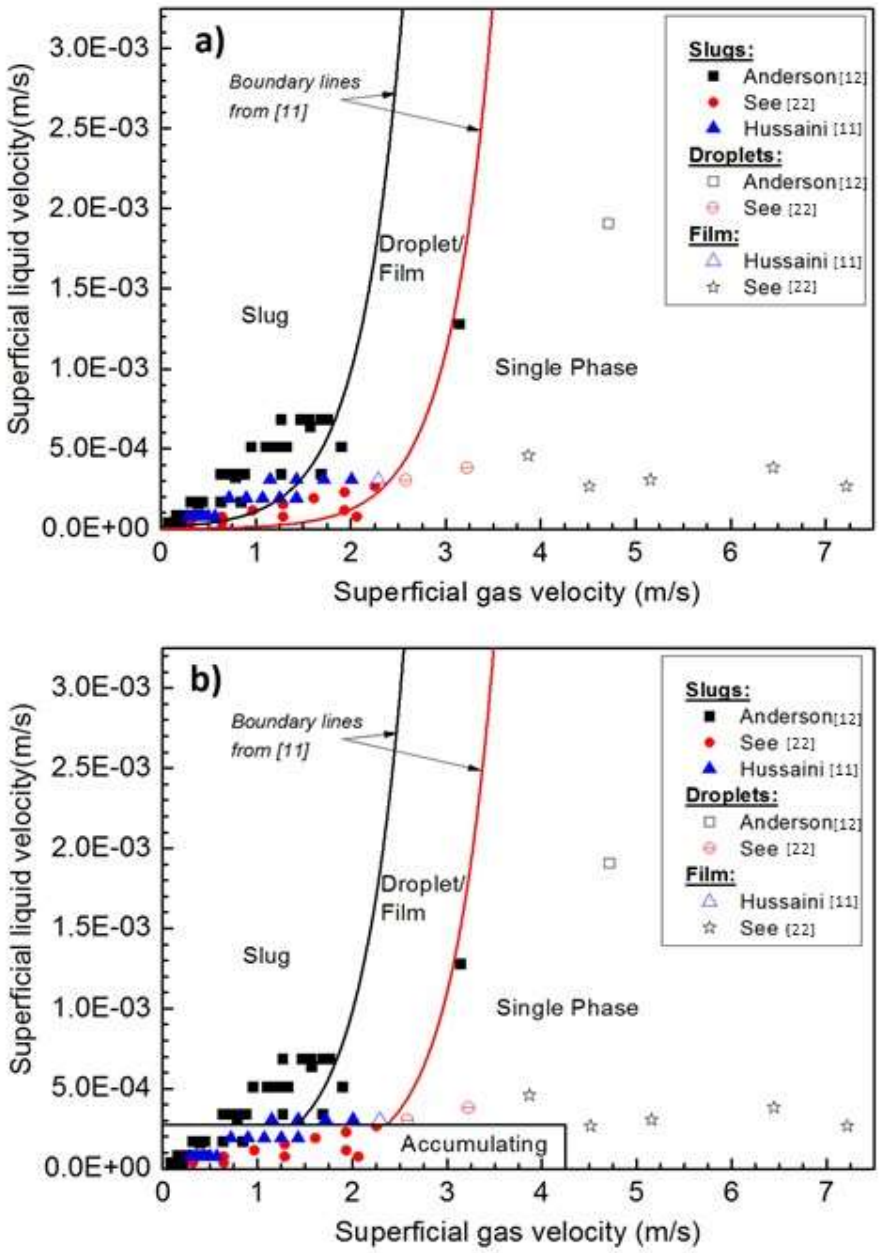

Figure 3.7 Predicted flow regimes from the force balance analysis compared to a) flow regime map boundaries from from Hussaini and Wang [11] and b) flow regime map boundaries from Anderson et al. [12].

The flow pattern maps are estimated based on visualization [11] and pressure drop analysis [12]. The agreement seems best suited for the prediction of the slug flow regime. In the original map in [11] the data show scatter between the observed flow patterns (e.g. droplets/film in the slug

region, slugs in the droplet/film region). These regimes were assigned via visual inspection, which is a subjective component common to many flow pattern maps. This could lead to error when comparing that map to the force balance. Considering of the all factors for water balance in the fuel cell is complex, thus the employed analysis here does not take into account the dynamic injection ports, differentiation of the GDLs with/without MPL, and possible condensation/evaporation effects. While considering these assumptions, the observed flow patterns are viewed at comparable (order of magnitude) gas and liquid flow rates as assigned via the force balance method presented here. Further, the force balance here predicts the onset of slugs or droplet flows. If those regimes are not noted, the assignment defaults to film flow as an assumption. Based on the results shown here, it may be more accurate to assign those cases to pseudo-single-phase flow/mist flow. These regions of low liquid velocity and high gas velocity may be harder to obtain data for as the flow rates are coupled via Faraday's Law. Thus, this region is only likely to be encountered in situations of high gas stoichiometry for parallel channel cells in this analysis.

The flow regime prediction above depends on not just the difference between the advancing and receding contact angles but also the magnitude of those angles. A sensitivity study was performed for data points assigned to each regime. In each case, the forces are recalculated based on advancing and receding contact angle pairs of 140° and 150°, 135° and 145°, 130° and 140°, 120° and 130°, and 110° and 120°. The percent change in the relevant force is noted in the table along with a new prediction of the flow regime. These results for liquid/gas systems in the slug, droplet, film, and single-phase regimes are shown in Table 3.4 and Table 3.5. Each table indicates the difference in advancing and receding contact angle (5°, 10°, and 20°), along with the absolute values used for the advancing and receding contact angles. The gas velocities shown are typical of

each groups' data. These tables indicate that as the difference in advancing and receding contact angle grows, the boundary for slug flow grows.

Table 3.3 Effect of advancing and receding contact angle magnitude and contact angle hysteresis applied to the data from Hussaini and Wang [11].

	$\theta_a - \theta_r = 5^o$		$\theta_a - \theta_r = 10^o$			$\theta_a - \theta_r = 20^\circ$		
Gas velocity [m/s]	135° & 130°	130° & 125°	140° & 130°	135° & 125°	130° & 120°	150° & 130°	145° & 125°	140° & 120°
0.57	Slug	slug	slug	slug	slug	slug	slug	slug
0.72	Slug	slug	slug	slug	slug	slug	slug	slug
0.9	Slug	slug	slug	slug	slug	slug	slug	slug
1.07	Slug	slug	slug	slug	slug	slug	slug	slug
1.25	Slug	slug	slug	slug	slug	slug	slug	slug
1.43	film	film	slug	slug	slug	slug	slug	slug
1.72	film	film	slug	slug	slug	slug	slug	slug
2.01	film	film	slug	slug	slug	slug	slug	slug
2.29	film	film	film	film	film	slug	slug	slug

Table 3.4 Effect of advancing and receding contact angle magnitude and contact angle hysteresis applied to the data from See [22].

	$\theta_a - \theta_r = 5^o$		$\theta_a - \theta_r = 10^o$			$\theta_a - \theta_r = 20°$		
Gas velocity [m/s]	135° & 130°	130° & 125°	140° & 130°	135° & 125°	130°& 120°	150° & 130°	145° & 125°	140°& 120°
0.322	Slug	Slug	slug	slug	slug	slug	slug	slug
0.645	Slug	Slug	slug	slug	slug	slug	slug	slug
0.967	Slug	Slug	slug	slug	slug	slug	slug	slug
1.289	Slug	Slug	slug	slug	slug	slug	slug	slug
1.611	Slug	Slug	slug	slug	slug	slug	slug	slug
1.934	droplet	droplet	slug	slug	slug	slug	slug	slug
2.256	droplet	droplet	slug	slug	slug	slug	slug	slug
2.578	droplet	droplet	slug	droplet	slug	slug	slug	slug
3.223	droplet	droplet	droplet	droplet	film	slug	slug	slug
3.868	droplet	film	film	film	film	droplet	droplet	film
4.512	droplet	film	film	film	film	film	film	film
5.157	droplet	film	film	film	film	film	film	film
6.446	film	film	film	film	film	film	film	film
7.219	film	film	film	film	film	film	film	film

3.4 Conclusions

In this work, an analytical approach is demonstrated to estimate which two-phase flow pattern is likely to occur in an operating PEM fuel cell. Analysis of the Damkohler number indicates that two-phase flow is likely based on the data sets in [11, 21, 22]. These data sets were specifically chosen because they contain active fuel cell data and two-phase flow multipliers. For each data set, the critical droplet size for detachment from the GDL surface was determined based on a force balance analysis. Once the critical droplet size is known, the forces for various flow regimes can be calculated, allowing the assignment of an expected flow pattern. Key conclusions include:

1. The critical droplet size is a function the superficial air velocity, contact angle, and contact angle hysteresis. Below the critical size, the droplet is considered stable and above this critical droplet size the droplet is unstable. Unstable droplets will detach from the GDL surface, and stable droplets will accumulate on the surface. A ratio of critical droplet diameter to channel size was determined. If this ratio if less than 1, the droplet will not detach due to contact with the remaining flow field walls.
2. The force estimates to determine the onset of slug, droplet, and film flow show reasonable qualitative agreement with the flow pattern maps in [11, 12]. The method reasonably predicts slug flow but film flow and single-phase flow are not well captured.
3. The regime assignment depends on contact angle and contact angle hysteresis. As the contact angle hysteresis grows, more gas and liquid flow rates are assigned to the slug flow regime.

3.5 Acknowledgments

LFZ and RA acknowledge the support from their respective universities, the University of

Saskatchewan and Montana State University. This collaboration was also supported under NSF Award number 1444198. PR also acknowledges Dean's Scholarship received from the University of Saskatchewan.

3.6 References

[1] T. A. Trabold, Minichannels in polymer electrolyte membrane fuel cells, Heat Transfer Eng. 26 (2005) 3-12.

[2] H. Li, Y. Tang, Z. Wang, Z. Shi, S. Wu, D. Song, A. Mazza, A review of water flooding issues in the proton exchange membrane fuel cell, J. Power Sources. 178 (2008) 103-117.

[3] W. Dai, H. Wang, X. Yuan, J. Martin, D. Yang, J. Qiao, J. Ma, A review on water balance in the membrane electrode assembly of proton exchange membrane fuel cells, Int. J. Hydrogen Energy. 34 (2009) 9461-9478.

[4] J. Bachman, M. Charvet, A. Santamaria, H. Tang, J. Park, R. Walker, Experimental investigation of the effect of channel length on performance and water accumulation in a PEMFC parallel flow field, International Journal of Hydrogen Energy. 37 (2012) 17172-17179.

[5] M. B. Burkholder, N. Siefert, S. Litster, Nonlinear analysis of voltage dynamics in a polymer electrolyte fuel cell due to two-phase channel flow, Journal of Power Sources. 267 (2014) 243-254.

[6] X. Liu, H. Guo, F. Ye, C. Ma, Water flooding and pressure drop characteristics in flow channels of proton exchange membrane fuel cells, Electrochimica Acta. 52 (2007) 3607-3614.

[7] F. Barbir, H. Gorgun, X. Wang, Relationship between pressure drop and cell resistance as a diagnostic tool for PEM fuel cells, Journal of Power Sources. 141 (2005) 96-101.

[8] M. Grimm, E. See, S. Kandlikar, Modeling gas flow in PEMFC channels: Part I–Flow pattern transitions and pressure drop in a simulated ex situ channel with uniform water injection through the GDL, International Journal of Hydrogen Energy. 37 (2012) 12489-12503.

[9] F. Barbir, PEM Fuel Cells: Theory and Practice, Elsevier Academic Press, Burlington (2005).

[10] R. Anderson, L. Zhang, Y. Ding, M. Blanco, X. Bi, D. P. Wilkinson, A critical review of two-phase flow in gas flow channels of proton exchange membrane fuel cells, Journal of Power Sources. 195 (2010) 4531-4553.

[11] I. Hussaini, C. Wang, Visualization and quantification of cathode channel flooding in PEM fuel cells, Journal of Power Sources. 187 (2009) 444-451.

[12] R. Anderson, R. E. Eggleton, L. Zhang, Development of two-phase flow regime specific pressure drop models for proton exchange membrane fuel cells, International Journal of Hydrogen Energy. 40 (2015) 1173-1185.

[13] T. Wu, N. Djilali, Experimental investigation of water droplet emergence in a model polymer electrolyte membrane fuel cell microchannel, Journal of Power Sources. 208 (2012) 248-256.

[14] C. Colosqui, M. Cheah, I. Kevrekidis, J. Benziger, Droplet and slug formation in polymer electrolyte membrane fuel cell flow channels: the role of interfacial forces, Journal of Power Sources. 196 (2011) 10057-10068.

[15] M. Cheah, I. Kevrekidis, J. Benziger, Water slug to drop and film transitions in gas-flow channels, Langmuir. 29 (2013) 15122-15136.

[16] M. Cheah, I. Kevrekidis, J. Benziger, Water slug formation and motion in gas flow channels: the effects of geometry, surface wettability, and gravity, Langmuir. 29 (2013) 9918-9934.

[17] A. Esposito, A. Montello, Y. Guezennec, C. Pianese, Experimental investigation of water droplet-air flow interaction in a non-reacting PEM fuel cell channel, Journal of Power Sources. 195 (2010) 2691-2699.

[18] S. Cho, Y. Wang, K. Chen, Droplet dynamics in a polymer electrolyte fuel cell gas flow channel: Forces, Deformation and detachment. II: Comparisons of analytical solution with numerical and experimental results, Journal of Power Sources. 210 (2012) 191-197.

[19] T. Hellstern, E. Gauthier, M. Cheah, J. Benziger, The role of the gas diffusion layer on slug formation in gas flow channels of fuel cells, International Journal of Hydrogen Energy. 38 (2013) 15414-15427.

[20] D. Ye, E. Gauthier, M. Cheah, J. Benziger, M. Pan, The effect of gas diffusion layer compression on gas bypass and water slug motion in parallel gas flow channels, AICHEJ. 61 (2015) 355-367.

[21] R. Anderson, D. Wilkinson, X. Bi, L. Zhang, Two-phase flow pressure drop hysteresis in an operating proton exchange membrane fuel cell, Journal of Power Sources. 196 (2011) 8031-8040.

[22] E. See, In situ measurement, characterization, and modeling of two-phase pressure drop incorporating local water saturation in PEMFC gas channels, M.S. thesis, Rochester Institute of Technology, Troy, NY (2013).

[23] S. Tsushima, S. Hirai, In situ diagnostics for water transport in proton exchange membrane fuel cells, Progress in Energy and Combustion Science. 37 (2011) 204-220.

[24] A. Bazylak, Liquid water visualization in PEM fuel cells: a review, Int. J. Hydrogen Energy. 34 (2009) 3845-3857.

[25] Z. Dunbar, R. Masel, Magnetic resonance imaging investigation of water accumulation and transport in graphite flow fields in a polymer electrolyte membrane fuel cell: Do defects control transport, J. Power Sources. 182 (2008) 76-82.

[26] J. Lee, J. Hinebaugh, A. Bazylak, Synchrotron X-ray radiographic investigations of liquid water transport behavior in a PEMFC with MPL-coated GDLs. J. Power Sources. 227 (2013) 123-130.

[27] S. Kim, S. Lee, A review on experimental evaluation of water management in a polymer electrolyte fuel cell using X-ray imaging technique, J. of Power Sources. 230 (2013) 101-108.

[28] Z. Lu, S. Kandlikar, C. Rath, M. Grimm, W. Domigan, A. White, T. Trabold, Water management studies in PEM fuel cells, Part II: Ex situ investigation of flow mal-distribution, pressure drop and two-phase flow pattern in gas channels, Int. J. Hydrogen Energy. 34 (2009) 3445-3456.

[29] Y. Wang, S. Basu, C. Wang, Modeling two-phase flow in PEM fuel cell channels, J. Power Sources. 179 (2008) 603-617.

[30] A. Bıyıkoğlu, Review of proton exchange membrane fuel cell models, Int. J. Hydrogen Energy. 30 (2005) 1181-1212.

[31] G. He, P. Ming, Z. Zhao, A. Abudula, Y. Xiao, A two-fluid model for two-phase flow in PEMFCs, J. Power Sources. 163 (2007) 864-873.

[32] E. Fontana, É. Mancusi, A. Ulson de Souza, S. Guelli Ulson de Souza, Flow regimes for liquid water transport in a tapered flow channel of proton exchange membrane fuel cells (PEMFCs), J. Power Sources. 234 (2013) 260-271.

[33] F. Jiang, C. Wang, Numerical modeling of liquid water motion in a polymer electrolyte fuel cell, Int. J. Hydrogen Energy. 39 (2014) 942-950.

[34] J. Carton, V. Lawlor, A. Olabi, C. Hochenauer, G. Zauner, Water droplet accumulation and motion in PEM (Proton Exchange Membrane) fuel cell mini-channels, Energy. 39 (2012) 63-73.

[35] A. Herescu, J. Allen, The influence of channel wettability and geometry on water plug formation and drop location in a proton exchange membrane fuel cell flow field, J. Power Sources. 216 (2012) 337-344.

[36] W. Yun, C. Ken, Elucidating two-phase transport in a polymer electrolyte fuel cell, Part 1: Characterizing flow regimes with a dimensionless group, Chem. Eng. Sci. 66 (2011) 3557-3567.

[37] C. Schillberg, S. Kandlikar, A review of modes for water droplet detachment from the gas diffusion later-gas flow interface in PEMFCs, In proceedings of the Fifth International Conference on Nanochannels, Microchannels and Minichannels, Puebla, Mexico, (2007) 299-310.

[38] J. Borrelli, S. Kandlikar, T. Trabold, J. Owejan, Water transport visualization and two-phase pressure drop measurements in a simulated PEMFC cathode minichannel, in ASME 3rd International Conference on Microchannels and Minichannels, American Society of Mechanical Engineers, June 13-15 (2005) 625-633.

[39] Z. Lu, A. White, J. Pelaez, M. Hardbarger, W. Domigan, J. Sergi, S. Kandlikar, Investigation of water transport in an ex-situ experimental facility modeled on an actual doe automotive target compliant fuel cell, in Sixth International Conference on Nanochannels, Microchannels and Minichannels, Darmstadt, Germany, June 23-25 (2008).

[40] E. Shirani, S. Masoomi, Deformation of a droplet in a channel flow. J. Fuel Cell Sci. Technol. 5 (2008) 041008.

[41] T. Murahashi, H. Kobayashi, E. Nishiyama, Combined measurement of PEMFC performance decay and water droplet distribution under low humidity and high CO, J. Power Sources. 175 (2008) 98-105.

[42] T. Ous, C. Arcoumanis, Visualisation of water droplets during the operation of PEM fuel cells, J. Power Sources. 173 (2007) 137-148.

[43] E. Kumbur, K. Sharp, M. Mench, Liquid droplet behavior and instability in a polymer electrolyte fuel cell flow channel, J. Power Sources. 161 (2006) 333-345.

[44] A. Theodorakakos, T. Ous, M. Gavaises, J. Nouri, N. Nikolopoulos, H. Yanagihara, Dynamics of water droplets detached from porous surfaces of relevance to PEM fuel cells, J. Colloid Interface Sci. 300 (2006) 673-687.

[45] C. Fang, C. Hidrovo, F. Wang, J. Eaton, K. Goodson, 3-D numerical simulation of contact angle hysteresis for microscale two phase flow, Int. J. Multiphase Flow. 34 (2008) 690-705.

[46] K. Chen, M. Hickner, D. Noble, Simplified models for predicting the onset of liquid water droplet instability at the gas diffusion layer/gas flow channel interface, Int. J. Energy Res. 29 (2005) 1113-1132.

[47] S. Cho, Y. Wang, K. Chen, Droplet dynamics in a polymer electrolyte fuel cell gas flow channel: Forces, deformation, and detachment. I: Theoretical and numerical analyses, J. Power Sources. 206 (2012) 119-128.

[48] L. Zhang, R. Anderson, An updated two-phase flow regime map in active PEM fuel cells based on a force balance approach, in ASME 2015 13th International Conference on Nanochannels, Microchannels, and Minichannels collocated with the ASME 2015 International Technical Conference and Exhibition on Packaging and Integration of Electronic and Photonic Microsystems, American Society of Mechanical Engineers, July 6–9 (2015) V001T03A011.

[49] J. LaManna, S. Kandlikar, Determination of effective water vapor diffusion coefficient in PEMFC gas diffusion layers, Int. J. Hydrogen Energy. 36 (2011) 5021-5029. [50] P. Gopalan, S. Kandlikar, Effect of channel material on water droplet dynamics in a PEMFC gas channel, J. Electrochem. Soc. 160 (2013) F487-F495.

[50] P. Gopalan, S. Kandlikar, Effect of channel material on water droplet dynamics in a PEMFC gas channel, J. Electrochem. Soc. 160 (2013) F487-F495.

[51] S. Kandlikar, E. See, R. Banerjee. Modeling two-phase pressure drop along PEM fuel Cell reactant channels. J. Electrochem. Soc. 162 (2015) F772-F782.

Chapter 4 - Investigation of time dependent water droplet dynamics on porous fuel cell material via Synchrotron Based X-ray imaging technique

The contents of this chapter have been submitted to the journal of **Experimental Thermal and Fluid Science** (Ms. Ref. No.: ETFS-D-17-00872).

Contribution of the MSc student

Experiments were planned by Paria Rahimian and Lifeng Zhang. Samples were prepared by both Paria Rahimian and Logan Battrell. Experiments were performed by Paria Rahimian with the assistance of Dr. Ning Zhu at the CLS.

Lifeng Zhang supervised and provided consultation during the entire experimental period as well as thesis preparation. All the writing of the submitted manuscript was done by Paria Rahimian with Lifeng Zhang and Ryan Anderson providing editorial guidance regarding the style and content of the paper.

Contribution of this chapter to the overall study

This chapter provides a good understanding of time dependent droplet behaviour including emergence, growth and detachment in a serpentine gas flow channel. The dynamics of growing droplets are visualized using synchrotron X-ray radiographic imaging. The whole growth pattern of the water droplet was detected and the cyclic evolution of dynamic contact angles and the height

and chord of a growing droplet are quantitatively analyzed. In addition, the critical detachment diameter of the droplets was compared to the predicted results of a theoretical approach.

4.1 Abstract

Proper water management in proton exchange membrane fuel cells (PEMFCs) remains a challenge, hindering the commercialization of this technology. Liquid water emerges in the form of droplets from micrometer-scaled pathways of porous gas diffusion layers (GDLs) into millimeter-scaled gas flow channels. Afterward, droplets grow to certain critical sizes before being removed by the convective gas flow. The opaque nature of fuel cell components, including GDL materials, poses significant challenges to understand droplet dynamics and develop more efficient water management techniques. In this work, an advanced synchrotron X-ray radiographic imaging technique available at the Canadian Light Source (CLS) was employed for the first time to visualize time dependent droplet behaviour in a serpentine PEMFC flow channel. High spatial and temporal resolution coupled with high energy photons of the X-ray beam provided high resolution images of growing droplets. From the captured images, the whole growth cycle of liquid droplets was obtained under various gas flow rates. A cyclic pattern of droplet dynamics including emergence, growth, and detachment was visualized from high resolution images. From the X-ray images, the evolution of dynamic contact angles and the height and chord of a growing droplet, were quantitatively analyzed. At higher gas velocities, the critical detachment diameter of the droplets became smaller and contact angle hysteresis was found be lower, while larger contact angle hysteresis and bigger droplets were observed at lower gas velocities. The critical droplet size at which the detachment of droplets occurred was compared to the predicted results from an analytical approach and good agreement was found.

Keywords: droplet dynamics, X-ray radiographic imaging, PEM fuel cell, water management, contact angle hysteresis

4.2 Introduction

Water is produced initially at the cathode catalyst layer of proton exchange membrane fuel cells (PEMFCs). After being pushed through the interconnected water pathways of porous gas diffusion layers (GDLs), liquid water can develop into droplet, film or slug flow regimes in the gas flow channels of the fuel cell depending on the flow conditions [1]. Since excess water can result in flooding and negative impacts on the fuel cell performance, high gas flow, typically air, in the cathode flow channels is needed to purge liquid water out of the cell. However, high superficial gas velocities result in significant parasitic power losses [2]. In order to find the optimal condition for removing excess water from the gas flow channels, a systematic study revealing how changing superficial gas velocity can influence liquid water behaviour is of great importance. Despite the importance, due to optical inaccessibility of both GDL and gas flow channels, liquid water behaviour including droplet evolution from emergence to detachment is still not well understood.

In terms of theoretical attempts and modeling, several research groups conducted studies on parameters controlling the formation and detachment of droplets [1-5]. In this regard, computational analysis was performed by Theodorakakos et al. [7] who investigated the droplet surface deformation to predict the actual shape of droplets sitting on three different GDLs using static and dynamic contact angles of droplets as an input for the volume of fluid (VOF) method. They indicated that droplet geometry altered dramatically from the initial static shape up to the point of detachment. Chen et al. [8] assumed spherical droplets to present their simplified model

based on macroscopic force balances and compared the results with experimental visualization data at low and high gas velocities. However, measuring the droplet aspect ratio at different gas velocities, Wu et al. [9] concluded that assuming a spherical shape for growing droplets in simplified models is very approximate due to hydrodynamic forces exerted by the gas flow. Zhu et al. [6] simulated the behaviour of droplets emerging through a micro-sized pore, which was followed by droplet growth and its interaction with a hydrophobic surface. Utilizing the VOF method, they investigated the effect of water connectivity inside a micro-sized pore on the critical detachment air velocity, which was significantly lower for the stagnant droplets sitting on the surface without pore pinning. However, information obtained from simulated gas flow channels as reported in the literature is different than actual conditions for operating fuel cells in several ways. In general, simulations in this field lack rigorous experimental validation. For instance, the pore is often imagined as a single injection port and the simulated surface does not exactly represent a true GDL [10-13]. Further, while a contact angle of a wall can be set, the models often do not include true variation in the contact line that can occur over time at the interface [13].

In terms of experimental attempts, the opaque nature of various components of PEM fuel cells poses significant challenges for visualisation of droplet behavior at the cathode side of PEMFCs. Bazylak et al. [14] presented a review paper on strengths and drawbacks of different visualization methods utilized in fuel cell studies including neutron imaging [15-20], NMR imaging [21-25], optical photography [11, 12, 26-31] and synchrotron X-ray imaging [32-34]. Minor et al. [35] utilized the micro-digital-particle-image-velocimetry (micro-DPIV) technique in optical photography to correlate air velocity with droplet deformation and contact angle hysteresis. They concluded that side-view optical images were not adequate to obtain concrete information regarding true interaction between the air-water interface for the air phase micro-DPIV method

and thus simultaneous top-view images were required as well. Using an optical visualization technique, Mortazavi et al. [36] found that due to the interconnected network of water pathways within GDLs, droplet emergence locations were totally random. In contrast, Yang et al. [37] pointed out that there were certain preferential locations for emerging droplets in gas flow channels. Bazylak et al. [38] concluded that preferential pathways existed, but these could shift over time, making it appear dynamic or random over longer timescales.

Although optical visualization of droplet behaviour could be possible through a clear plate from the top-view, capturing the evolution of a growing droplet in terms of dynamic contact angles and the critical height of droplet is required to be from the side. Considering the preferential emergence of droplets in random locations in serpentine or parallel channels, side-view optical visualization is not feasible due to channel overlapping in parallel or serpentine flow fields. Also, different flow regimes that occur simultaneously along the serpentine channels due to non-uniform water emergence between the inlet and outlet of long channels cannot be captured separately for the same reason [39].

Synchrotron based X-ray imaging as a result of high energy penetrating photons plus high spatial and temporal resolution makes the observation of multiphase flow within the length of a serpentine channel feasible. Lee et al. [40] employed synchrotron X-ray radiography to compare the liquid water transport through GDLs with and without microporous layers (MPL). They reported that GDLs assembled with MPL could prevent flooding due to the nano-scaled pores of MPL, which could result in smaller water clusters and lower water saturation of the GDL. Also, Manke et al. [41] used synchrotron X-ray imaging techniques to investigate liquid water evolution and transport through GDLs in gas flow channels of an operating fuel cell. Based on a quantitative

analysis of water development, they found a dynamic equilibrium between droplets in the channel and water clusters in the GDLs.

The dynamic contact angle of droplets during the droplet flow regime is a key factor for fuel cell water management, and it is determined by interfacial energy along the three-phase boundary. Drag force, surface adhesion force and capillary pressure have an influence on the dynamic contact angles of droplets on the GDL surface. Surface adhesion force resulting from solid-liquid molecular interactions makes growing droplets adhere to a solid surface by overcoming the drag force imposed by the gas flow [36]. Nevertheless, drag force makes the advancing and receding contact angles of the droplet different from the static contact angle, and the resulting difference between advancing and receding contact angle is termed "contact angle hysteresis". Kumbur et al. [5] noted that contact angle hysteresis was a function of droplet size, superficial gas velocity and contact surface properties.

In the literature, though a few attempts of using X-ray radiographic imaging techniques have been made to understand liquid transport in PEMFCs, specific attention on time dependent droplet behaviour, particularly, droplet growth cycles and dynamic contact angles, was very limited. In particular, dynamic contact angles and contact angle hysteresis are much needed information for numerical modeling and simulations where static contact angles are often used. Therefore, in view of this knowledge gap, the main objectives of the current work were to understand droplet dynamics through advanced X-ray radiographic imaging techniques and to provide information on dynamic contact angles during droplet growth. The focus of this study is on how droplet hysteresis is 1) varying with time and 2) cyclical. This work shows how long it takes for a droplet to reach certain advancing and receding contact angles, and how this process is noted by multiple, distinct 'phases' of contact angle behavior before detachment. To the point above, this behavior is not

analyzed in computational fluid dynamics (CFD) simulations. In addition, the experimental results of critical droplet sizes were compared to those predicted from an analytical approach previously developed [8]. This work provides valuable insight into the evolution and instability of growing droplets and suitable quantitative data to verify numerical analyses and theoretical models.

4.3 Experimental section

The ex-situ fuel cell used in this work was designed for synchrotron X-ray visualization of experiments on dynamics of liquid water at the cathode side of a fuel cell. In-plane X-ray visualization was conducted while the direction of X-ray beam was horizontally parallel to the GDL plane. The following sections detail the test cell design, experimental conditions and synchrotron radiography setup.

4.3.1 Microchannel design

The microfluidic device (i.e. ex-situ fuel cell) fabricated specifically for these experiments includes a serpentine channel with dimensions of 0.5 mm×1 mm. The reason for opting for a serpentine channel was to increase the probability of capturing droplet growth cycles in different parts of the gas flow field. To represent the actual droplet emergence phenomena relevant to PEMFC operation, instead of using a single water injection pore, liquid water emerges from a Sigaret 25 BC GDL ensuring the pore size and emergence locations are randomly distributed. The uncompressed GDL is loaded with 5%wt polytetrafluoroethylene (PTFE), assembled with a MPL, and has a thickness of 235 μm and air permeability of 1 $cm^3/(cm^2 \cdot s)$.

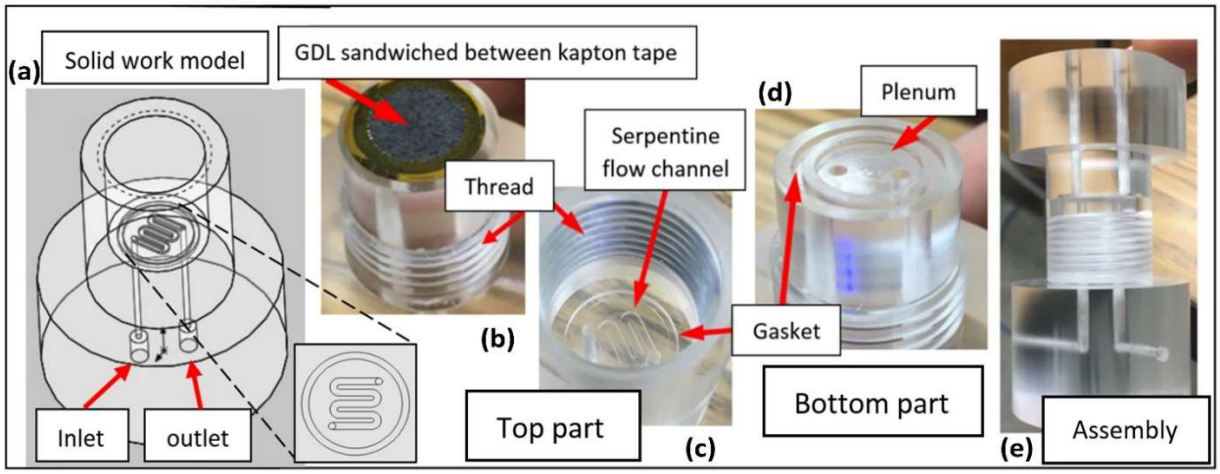

Figure 4.1. Top part, bottom part and the assembly of acrylic test cell with a single serpentine channel: (a) the overall view of the set-up; (b) Bottom half with GDL; (c) Top half of the test cell; (d): Bottom half without GDL; (e) The assembly. The image of test cell mounted on stage in BMIT beamline at the CLS is provided in appendix D and the solid work scheme of test cell is provided in appendix F.

Figure 4.1 shows the acrylic test cell with a single serpentine micro-channel with the length of 35 mm simulating an operating PEM fuel cell with active area of 1.32 cm^2. Acrylic is selected as it minimizes X-ray beam attenuation vs. a fuel cell material like graphite. Figures 4.1b and 4.1d show the bottom half of the test cell with and without the GDL. The bottom part contained a plenum (0.5mm depth) where water was injected. Figures 4.1a and 4.1c show the top part containing the engraved serpentine channel. Figure 4.1e shows the assembly of the ex-situ fuel cell. The two halves were designed to be screwed together with a GDL separating them. The GDL was placed over a silicone rubber gasket to prevent any possible leakage from the channel. The acrylic fuel cell mounted on stage in the BMIT beamline hutch is shown in Appendix D.

4.3.2 Experimental conditions

Both air and deionized water were used as fluids in the experiments and the test cell was operated at ambient conditions ($T = 25°C$ and $P = 1$ atm). The liquid water flow rate was controlled by a syringe pump (NE-1000, New Era Pump Systems Inc., USA) with a maximum flow capacity

of 1699 ml/hr. Air was supplied through a pressurized air cylinder with a mass flow meter (FL-3802ST, Omega, Canada) with a maximum flow rate of 814 ml/min. The flow conditions were scaled to relevant fuel cell operations. The superficial velocities were based on the set volumetric flow rates and cross-sectional area of the serpentine flow channel. Air superficial gas velocities included 4.2, 5.5 8.3, and 10.3 m/s, corresponding to air Reynolds numbers of 179, 228, 357, and 443. The superficial water velocity was 0.001 m/s in all cases.

4.3.3 Synchrotron radiography setup

Experiments were performed at 05B1-1 beamline at the Biomedical Imaging and Therapy (BMIT) facility at the Canadian Light Source (CLS), which is a 2.9 GeV third generation synchrotron. White beam (polychromatic beam) was used for the visualization of water droplet dynamics and the beam was parallel to the GDL direction (in-plane imaging). The images obtained from BMIT include both X-ray absorption contrast and phase contrast. An optimal sample-to-detector distance was set at 50 cm to obtain additional phase contrast, which enhances the edge of the water droplets and makes contact angle analysis more accurate. The projected images were recorded by means of a beam monitor AA-40 (10 μm GSO scintillator, Hamamatsu, Japan) coupled with a camera (Hamamatsu ORCA Flash 4.0, Japan) with an effective pixel size of 6.4 μm. The detector field of view was 13x13 mm^2. To capture motion of water droplets in real time, a sequence of 500 projection images was captured with a frame rate of 7.7 FPS at each condition. Raw images obtained were composed of gray-scale values. Digital image post processing was done utilizing a BMIT toolbox plugin in ImageJ software. In order to detect the formation and accumulation of liquid water in the flow channel, Beer-Lambert's law was applied to raw X-ray images. Beer-Lambert's law correlates the attenuation of X-ray to the thickness of material through which the

beam is traveling. Wet state X-ray images containing liquid water are normalized using dry state images and the normalization procedure was explained by Hinebaugh et al. [44].

4.4 Results and discussion

Static contact angles the droplet made with acrylic and 5% PTFE loaded carbon paper are summarized in Table 4.1 Dynamic advancing and receding contact angles were measured via the sessile droplet goniometer method, which determines the largest and smallest contact angles possible for a droplet without changing its solid-liquid interfacial contact line [43]. The maximum contact angle made by adding to the droplet volume dynamically is the dynamic sessile advancing contact angle (θ_{SA}) and the minimum possible contact angle of droplet by removing from the droplet volume is the dynamic sessile receding contact angle (θ_{SR}). The method of contact angle measurement is provided in appendix C.

Table 4.1. Static and dynamic contact angles of water with channel walls and base GDL with measured with the sessile droplet method.

Surface	Static Sessile Contact Angle (°)	Dynamic Sessile Advancing Contact Angle (°)	Dynamic Sessile Receding Contact Angle (°)
Carbon paper (5% PTFE loaded)	111	121	57
Acrylic	46	55	24

4.4.1 Evolution of dynamic contact angles

Radiographic X-ray images were analyzed frame by frame to elucidate the evolution of the contact angle of the droplets from emergence up to the detachment. Representative results are shown in Figures 4.2 and 4.3 for two different velocities, u_g = 4.2 m/s and u_g = 10.3 m/s, respectively. As seen in Figure 4.2, there are four different phases during the evolution of θ_a, θ_r and the contact angle hysteresis (θ_a- θ_r) of the droplets during emergence up to the detachment at u_g = 4.2 m/s.

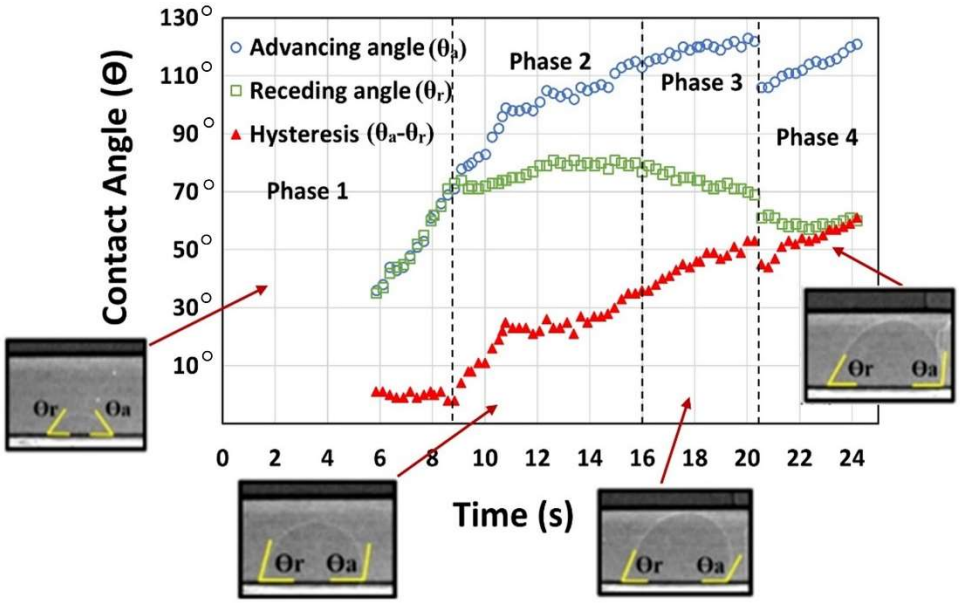

Figure 44.2 Evolution of advancing contact angle, receding contact angle, and contact angle hysteresis (u_g = 4.2 m/s and u_l = 0.001m/s).

In Phase 1 (0-9 s), droplets emerge and surface adhesion is the dominant force. In this phase, the growth rates for θ_a and θ_r are similar (12.8°/s) and the contact angle hysteresis is zero, resulting in a symmetric shape of emerging droplets. In Phase 2 (9-16 s), due to the larger exposure area of the growing droplets, the shape of the the droplets is deformed in response to the drag force in the direction of gas flow by increasing θ_a at a higher rate compared to θ_r (4.9°/s for θ_a versus 1.5°/s

for θ_r). Hence, an initial growth in contact angle hysteresis can be observed in this transition zone which corresponds to Phase 2 in Figure 4.2. In Phase 3 (16-20.8 s) when the droplet height reaches 0.38 mm, θ_r starts to decrease while θ_a still increases with time. As a result, the contact angle hysteresis increases at a very high rate (3.9°/s), inducing a significant deformation of the droplet.

Finally, entering Phase 4 (20.8-24.3 s), a sudden drop in θ_a, θ_r, and contact angle hysteresis takes place. This sudden change coincides with the droplet height reaching the height of the channel (0.5 mm in the current experimental set-up) and a simultaneous drop in contact angle hysteresis from 53° to 45°. Afterwards, the contact angle hysteresis starts to grow again until reaching a maximum of 61° before droplet detachment at the end of Phase 4. At detachment, the droplet grows to a maximum height of 0.5 mm. Detailed discussion about the coincidence in this phase is presented in the following section with respect to the evolution of the height and chord of a droplet over time.

Figure 4.3 presents the evolution of a gradual trend of dynamic contact angles at u_g = 10.3 m/s. Unlike the previous condition (u_g = 4.2 m/s), droplets exposed to superficial gas velocity of 10.3 m/s only experience two phases before being purged out of the channel. Additionally, drops have a fixed shape for a long period of time. During the Phase 1, the curves for advancing and receding contact angles overlap with each other, resulting in a symmetric shape of a droplet for 12 s, nearly half of the cycle. As the cycle progressed toward detachment during Phase 2, contact angle hysteresis reaches 22°, much lower than the maximum contact angle hysteresis of droplets at u_g = 4.2 m/s (62°), indicating that droplets at high velocities are more symmetrical.

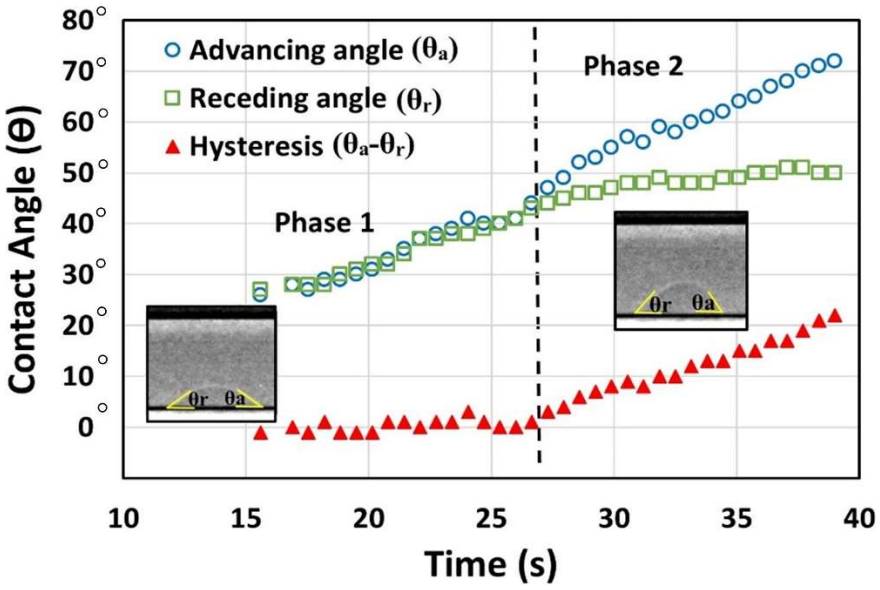

Figure 4.3 Evolution of advancing contact angle, receding contact angle, and contact angle hysteresis (u_g = 10.3 m/s, u_L = 0.001 m/s).

4.4.2 Cyclic behavior of the height and chord of a droplet

From the captured X-ray images, droplet height and chord were measured. Figures 4.4 and 4.6 present the height and chord of a single droplet being generated and ejected from the GDL surface at two superficial gas velocities, u_g = 4.2 m/s and 10.3 m/s, respectively. The droplet growth cycle is only shown for the first 80 s for brevity. From the figures, a cyclic process in which droplets grow to a critical size and detach from the GDL surface is observed. As can be seen in Figure 4.4, the droplet grows to a critical height close to the channel height (0.5 mm in the present work) before detachment at u_g = 4.2 m/s. In contrast, at u_g = 10.3 m/s, the droplet only grows to 0.25 mm. It can be seen that one cycle is approximately 18 s for u_g = 4.2 m/s and the average droplet growth rate is 0.024 mm/s. In Figure 4.4, the region marked by dashed lines details four distinct moments of one repeated cycle of the droplet growth at the surface of the GDL.

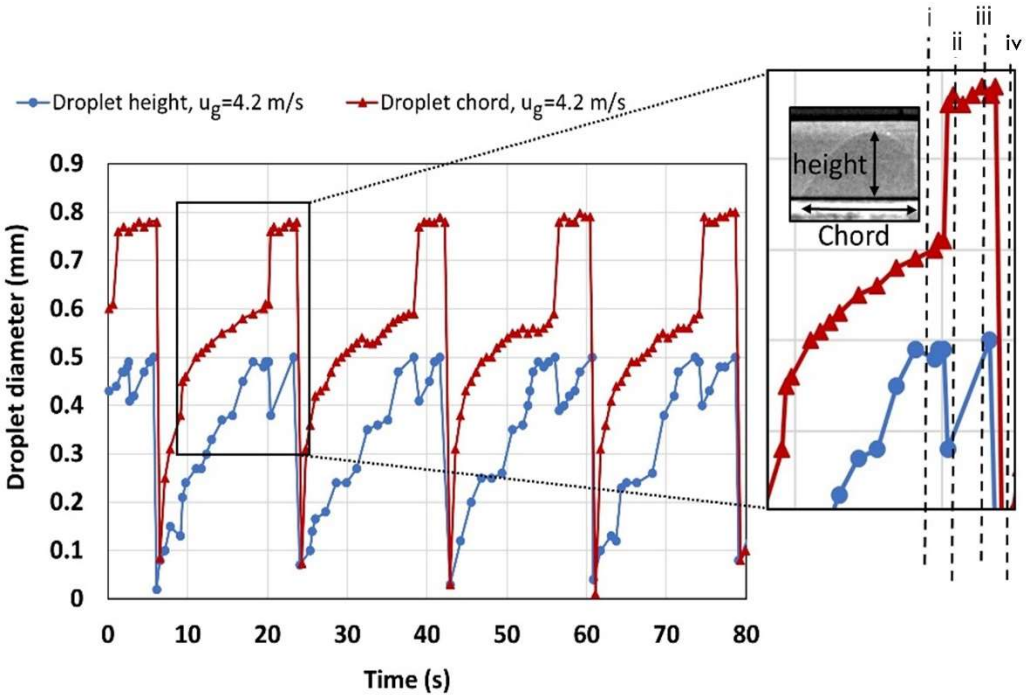

Figure 4.4 Cyclic behavior of the droplet growth in terms of height and chord at u_g = 4.2 m/s.

In a typical growth cycle, there is a gradual growth stage (marked i as shown in the box in Figure 4.4) for both droplet height and chord. When the droplet height reaches the height of the channel, a sharp decrease in the droplet height is observed at the moment of contact (marked as ii). This sudden decrease in the droplet height is accompanied with a sharp increase in the droplet chord. This is reasonable from the mass balance point of view. At this point, the drag forces exerted by the gas flow are still not high enough to purge the droplet out of the channel. However, the location of the droplet is moved by about 1.2 mm along the direction of the air flow, as indicated in Figure 4.5 (Image 6 at t = 23.4 s). The ratio of the droplet chord to height, a measure of droplet elongation, abruptly increases from 1.2 to 1.9. The droplet extension can also be appreciated in Figure 4.2 when the dynamic contact angle curve enters Phase 4 at t = 20.8 s and the contact angle hysteresis drops sharply. This phenomenon can be accounted for by the differential pressure between the upstream and downstream of the droplet. As the droplet grows and the droplet height increases, it

reduces the channel cross-section and the gap through which air flows in the channel shrinks. Images 1-4 in Figure 4.5 indicate that $H_{gap1} > H_{gap2} > H_{gap3} < H_{gap4}$. Any decrease in this gap results in an increase in the gas velocity in the remaining open area of the channel and further increase in differential pressure for the flow through the gap. Hence, θ_r decreases and θ_a increases gradually. The advancing and receding contact lines of the droplet remain pinned to the GDL surface until either $\theta_r < \theta_{DSR}$, leading to advancing contact line motion, or $\theta_a > \theta_{DSA}$, leading to receding contact line motion [42].

When the advancing contact angle exceeds the dynamic sessile advancing contact angle but the receding contact angle does not go below the dynamic sessile receding contact angle, the drag force imposed by the gas flow exceeds the force required for the moving advancing contact line of the droplet and thus the upstream contact line makes a sudden advancement toward the outlet whereas the receding contact line remains pinned to the GDL surface [1]. There are three resultant consequences:

1. The droplet is elongated in the air flow direction and the droplet chord increases;
2. The advancing contact angle and the contact angle hysteresis decrease;
3. The droplet height contracts and the gap between the channel walls through which the air can flow increases.

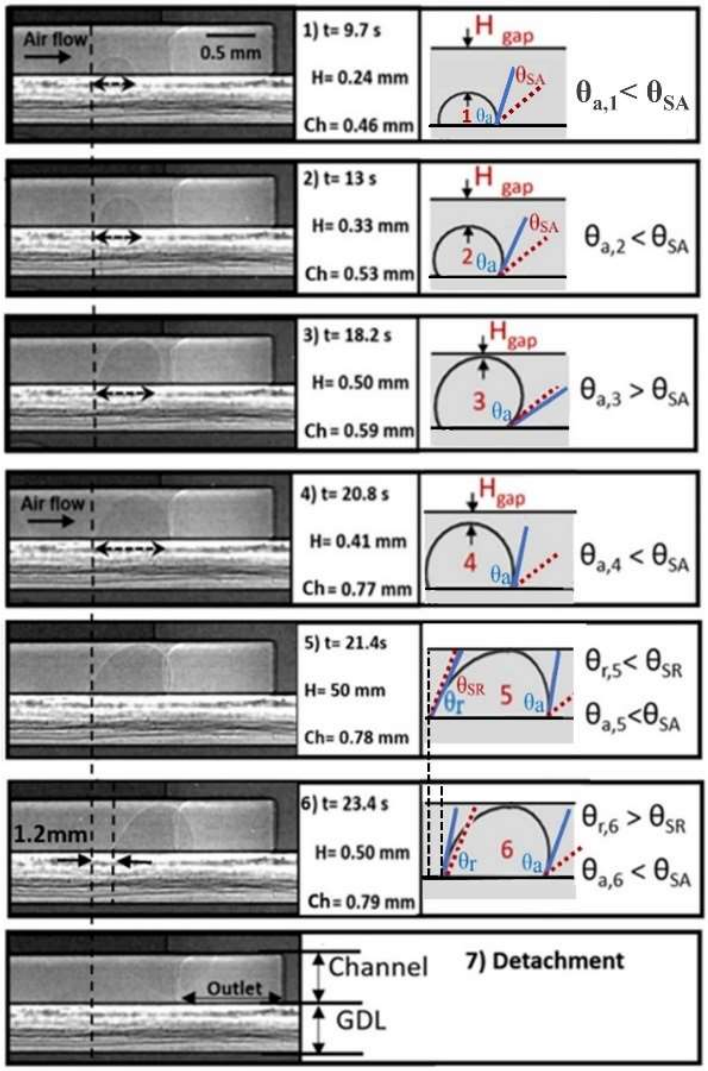

Figure 4.5 Visualization of droplet dynamics (emergence, growth and detachment) at u_g = 4.2 m/s and u_l = 0.001 m/s (side view images). The black dashed line in the image sequence is placed to guide the eyes for droplet emergence location. The distance between emergences to detachment location is ~1.2 mm.

This phenomenon is clearly depicted by a sequence of X-ray images in Figure 4.4, where the droplet diameter drops to 0.41 mm after contacting the channel wall. Images 3 and 4 in this figure clearly show the sudden increase in the droplet chord to height ratio and simultaneous decrease in the contact angle hysteresis.

Another interesting observation here is detachment and stalling of the droplet occurring in Images 5 and 6 in Figure 4.5. As shown in Images 1-4, the droplet growth takes place while the

upstream contact line remains pinned to the pore site and the downstream contact line gradually advances toward the channel outlet. As the downstream contact line progresses, the receding contact angle decreases. Also, the force exerted by the gas flow does not exceed the force required for the droplet motion and thus the droplet remains pinned to the emergence location.

However, the droplet relocation can be observed at t = 23.4 s where $\theta_{SR} > \theta_r$ and $\theta_{DA} > \theta_a$. At this point, the forces imposed by the gas flow are higher than the force for moving the receding contact line of the droplet but are not high enough for moving the advancing contact line. Hence, the droplet detaches and stalls. Cheah et al. [1] reported a theoretical explanation on this in hydrophobic channels at low superficial gas velocities, which is confirmed by the current findings.

Thereafter, the droplet height again continues growing until it reaches the critical height of 0.5 mm for the second time while the droplet chord remains constant as it is marked by iii in Figure 4.4. As a result, the contact angle hysteresis continues to increase to 61° one frame prior to droplet detachment. Eventually at t = 24.3 s, the resultant pressure difference is high enough to overcome the force required for the droplet motion and remove the droplet from the GDL surface (as marked by iv in Figure 4.4). Image 7 in Figure 4.5 indicates that the downstream contact line detaches first and ultimately the upstream contact line detaches, leading to the droplet detachment from the channel. After droplet detachment, different flow patterns might occur in the gas flow channel. Different flow patterns were observed using X-ray imaging technique and the detailed analysis is provided in appendix A.

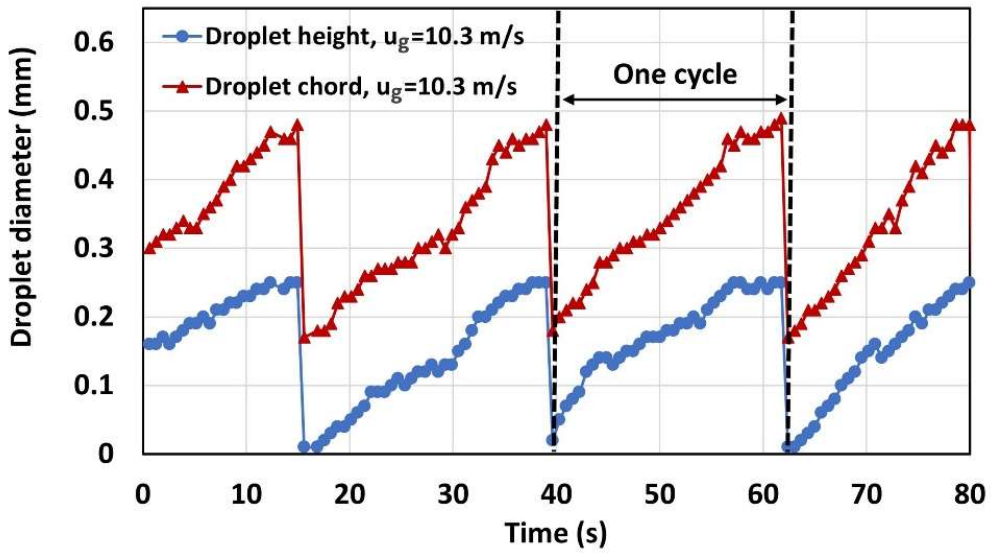

Figure 4.6 Cyclic behavior of the droplet growth in terms of height and chord at u_g = 10.3 m/s.

At a high superficial gas velocity of 10.3 m/s as shown in Figure 4.6, the droplet detachment height and chord are only about 0.25 mm and 0.48 mm, respectively. In this case, the drag forces exerted by the gas flow are high enough to remove the droplet before it reaches the channel height. Hence, the droplet aspect ratio (height/chord) at the moment of detachment is approximately 0.5, implying that in higher gas velocities droplets have a more hemispherical shape. Kumbur et al. [5] proposed the assumption of symmetrical and hemispherical droplets in their model predicting contact angle hysteresis of droplets in an unstable state. The current findings indicate that this assumption shall be carefully used at low gas velocities.

4.4.3 Comparisons of critical droplet sizes with analytical predictions

As discussed in previous sections, when emerging droplets grow to their critical detachment size they become unstable and ready to detach from the GDL surface. If the droplet's critical detachment diameter is larger than the channel diameter, the droplet will obstruct the whole cross

section area of the channel, resulting in slug flow. Hence, the detachment diameter of growing droplets is a key factor for designing gas flow channels of PEMFCs [36].

An analytical approach based on a force analysis for predicting critical droplet sizes was employed by several groups [4, 44, 45]. The detailed procedure is available in Cho et al. [4]. The predicted critical droplet diameter was compared to the results from X-ray images. The results are shown in Table 4.2. It can be seen that with an increase in the gas velocity, the critical droplet size decreases. This trend is observed in both predicted values and experimental results. The relative deviation between the experimental results and theoretical values is within 12%, indicating reasonably good agreement. The deviation might arise from the assumption of a single droplet in the analytical approach [4]. The uncertainty measurements for critical droplet diameters are provided in appendix E.

Table 4.2 Critical droplet diameters at different gas velocities.

Superficial gas velocity, u_g, m/s	Reynolds number, $Re_g = \frac{\rho u_g H_{d*}}{\mu}$	Critical droplet diameter (analytical), mm	Critical droplet diameter (from X-ray images), mm	Relative deviation, %
4.2	179	0.45	0.49	8
5.5	228	0.36	0.41	12
8.3	357	0.31	0.32	3
10.3	443	0.22	0.25	12

*ρ is the density of the fluid (SI units: kg/m^3), u is the velocity of the fluid with respect to the object (m/s), L is a characteristic linear dimension (m), μ is the dynamic viscosity of the fluid (Pa·s or N·s/m2 or kg/m·s)

The dependence of contact angle hysteresis and droplet height/chord ratio at the onset of detachment on superficial gas velocities is shown in Figure 4.7. The height/chord ratio values could be interpreted as a measure of droplet hemisphericity. Contact angle hysteresis is a measure of the droplet's ability to resist the drag force exerted by the gas flow, which deforms the droplet asymmetrically [11]. As can be seen in this figure, increasing the superficial gas velocity causes the ratio of droplet height against chord to decrease close to 0.5, implying that droplets tend to be more hemispherical at detachment for higher superficial gas velocities. Similarly, results from Figure 4.7 confirm a symmetrical and hemispherical droplet shape by noting that the dynamic contact angles of a growing droplet at a high superficial gas velocity only experience two phases with the maximum contact angle hysteresis of 22° before droplet detachment. Therefore, the assumption of hemispherical droplets in many simulations and simplified hemispherical-droplet models predicting the droplet behavior could lead to errors at low superficial gas velocities.

In addition, increasing the gas velocity leads to a decrease in the contact angle hysteresis at the point of detachment. As the gas velocity increases, the critical detachment height of the droplets decreases. Smaller droplets deform less due to lower differential pressure forces between the upstream and downstream surfaces of the droplet, resulting in a lower contact angle hysteresis.

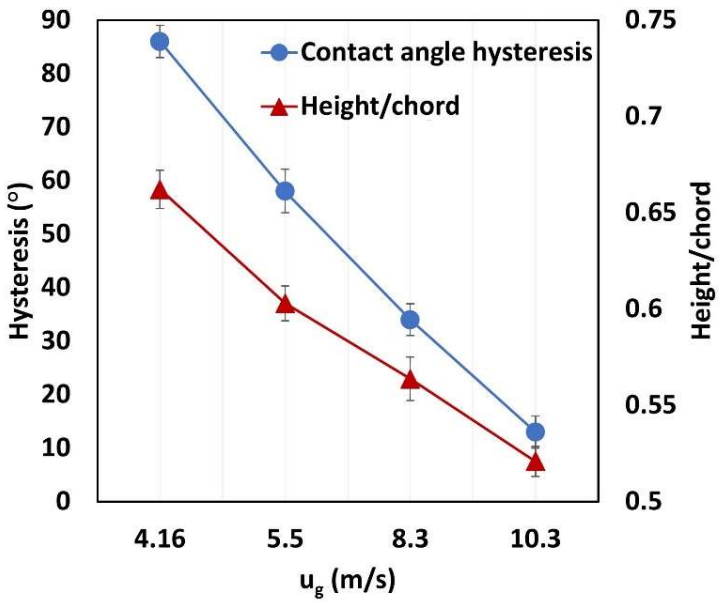

Figure 4.7 Effect of superficial air velocity on contact angle hysteresis and droplet aspect ratio at the point of droplet detachment. (Error bars represent the relative error of three times measurements for each data point).

Figure 4.8 shows the onset of instability causing droplet detachment while exposed to a pressure gradient exerted by the gas stream. The simplified model predicting the droplet instability based on contact angle hysteresis and height of droplets proposed by Chen et al. [44] is compared with experimental data at three different air velocities. The detailed procedure of the numerical analysis to obtain the dimensionless height of the droplet (droplet height/channel height) as a function of contact angle hysteresis is available in Chen et al. [44]. Based on the suggested equation by Chen et al. [44], the analytical solution for the critical droplet sizes defines the boundary between two regions for stable and unstable droplets. Below the critical droplet size, stable droplets remain pinned to the GDL surface by surface tension forces. In contrast, any droplet reaching the critical droplet size becomes unstable and will detach from the GDL surface by the convective gas flow. Detachment of unstable droplets occurs either by shear force exerted by gas flow in high gas velocities or by corner flow through capillary wicking of water into channel side walls in low gas

velocities. The detailed analysis of droplet-side wall interactions using cross sectional X-ray images is provided in appendix B.

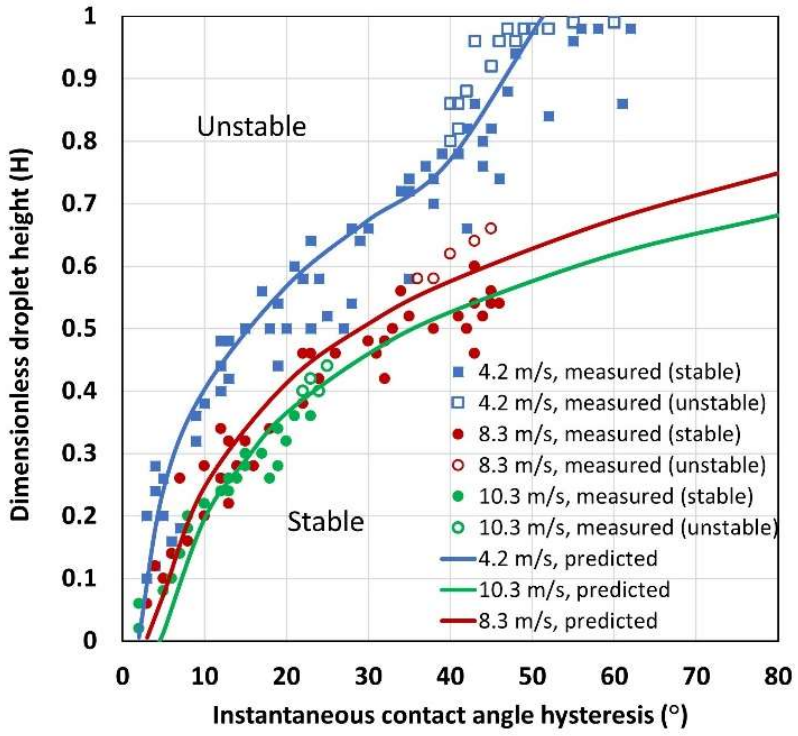

Figure 4.8 Comparison of predicted droplet instability with experimental observations at two air velocities.

In Figure 4.8, boundary lines for three velocities are generated and experimental data were also compared. As indicated in Figure 4.8, the dimensionless droplet height is a function of contact angle hysteresis. As the droplet height increases and the gap through which gas flows decreases and the droplet is subjected to greater differential pressure force of the gas flow, hence the droplet shape is deformed to minimize the pressure gradient experienced by the upstream and downstream sides of a droplet. X-ray images in Figure 4.5 clearly indicate that the shape of the droplets is changed more as they obstruct more of the cross section of the gas flow channel and they become unstable entering the last phase of contact angle evolution. At larger contact angle hysteresis, the

droplet height is higher, indicating larger stable droplets. The observation is consistent with the previous discussion. In addition, it can be observed that increasing the superficial air velocity enlarges the droplet-instability window, thereby enhancing the droplet removal. Generally, a reasonable qualitative trend can be observed for both the simplified model and the experimental data. However, as Chen et al. [45] mentioned there are several reasons for the discrepancy between the predicted and measured droplet instability window. Among these, assumptions of a single spherical droplet and flow in the gap above the droplet as parallel plates are considered to account for the discrepancy observed.

4.5 Conclusions

In this work, the synchrotron based X-ray imaging technique was used to explore time varying droplet dynamics in a flow channel related to PEM fuel cell operation for the first time. Evolution of dynamic contact angles, height and chord of a growing droplet was visualized from the X-ray images captured. In the cyclic behaviour observed from the X-ray images, a droplet grows while it is pinned to the emergence location until the force exerted by gas flow is sufficiently large for advancing the liquid-solid contact line of the droplet. Stick-slip motion of advancing and receding contact lines of growing droplet corresponds to the dynamic contact angles of droplets. High resolution sequential X-ray images also indicate shedding and stalling of droplets in every cycle before detachment when the contact angle hysteresis and droplet aspect ratio show a sudden change. By increasing the gas flow rates, both the contact angle hysteresis and droplet aspect ratio decrease, making the droplet shape more symmetrical and spherical at the moment of detachment. Therefore, the assumption of hemispherical droplets in simulations and simplified hemispherical-

droplet models is more realistic at high gas flow rates. Increasing air velocity enlarges the droplet instability window. Thus, smaller droplets are capable of detaching at higher air velocities.

The current study provides a complete picture of time dependent droplet behaviour including emergence, growth, and detachment in flow channels with limited optical access. In the numerical modeling, hemispherical assumptions need to be revisited, especially, at low gas flow rates where large contact angle hysteresis is observed. In addition to applications in PEM fuel cell water management, the results and technical methods can be extended to other microfluidic devices where droplets are of practical interest and optical access is a challenge.

4.6 Acknowledgments

LFZ and RA acknowledge the support from their respective universities, the University of Saskatchewan and Montana State University. This collaboration was also supported under NSF Award number 1444198. LFZ and PR also acknowledge Dean's Scholarship received from the University of Saskatchewan and financial support from Natural Sciences and Engineering Council of Canada (NSERC). The research described in this paper was performed at the BMIT facility at the Canadian Light Source, which is supported by the Canada Foundation for Innovation, Natural Sciences and Engineering Research Council of Canada, the University of Saskatchewan, the Government of Saskatchewan, Western Economic Diversification Canada, the National Research Council Canada, and the Canadian Institutes of Health Research.

4.7 References

[1] M. J. Cheah, I. G. Kevrekidis, J. B. Benziger, Water Slug to Drop and Film Transitions in Gas-Flow Channels. Langmuir, 29 (2013) 15122–15136.

[2] F. Y. Zhang, X. G. Yang, C. Y. Wang, Liquid Water Removal from a Polymer Electrolyte Fuel Cell. J. Electrochem. Soc.,153 (2006) A225.

[3] M. J. Cheah, I. G. Kevrekidis, J. B. Benziger, Water Slug Formation and Motion in Gas Flow Channels: The Effects of Geometry, Surface Wettability, and Gravity. Langmuir, 29 (2013) 9918–9934.

[4] S. Chan, Y. Wang, K. S. Chen, Droplet Dynamics in a Polymer Electrolyte Fuel Cell Gas Flow Channel: Forces, Deformation and Detachment. II : Comparisons of Analytical Solution with Numerical and Experimental Results. J. Power Sources, 210 (2012) 191–197.

[5] E. C. Kumbur, K. V. Sharp, M. M. Mench, Liquid Droplet Behavior and Instability in a Polymer Electrolyte Fuel Cell Flow Channel. J. Power Sources, 161 (2006) 333–345.

6] X. Zhu, P. Sui, N. Djilali, Dynamic Behaviour of Liquid Water Emerging from a GDL Pore into a PEMFC Gas Flow Channel. J. Power Sources, 172 (2007) 287–295.

[7] A. Theodorakakos, T. Ous, M. Gavaises, J. M. Nouri, N. Nikolopoulos, H. Yanagihara, Dynamics of Water Droplets Detached from Porous Surfaces of Relevance to PEM Fuel Cells. J. Colloid Interface Sci., 300 (2006) 673–687.

[8] K. S. Chen, M. A. Hickner, D. Noble, Simplified Models for Predicting the Onset of Liquid Water Droplet Instability at the Gas Diffusion Layer/gas Flow Channel Interface. Int. J. Energy Res., 29 (2005) 1113–1132.

[9] T. C. Wu, N. Djilali, Experimental Investigation of Water Droplet Emergence in a Model Polymer Electrolyte Membrane Fuel Cell Microchannel. J. Power Sources, 208 (2012) 248–

256.

[10] X. Zhu, P. C. Sui, N. Djilali, Three-Dimensional Numerical Simulations of Water Droplet Dynamics in a PEMFC Gas Channel. J. Power Sources, 181 (2008) 101–115.

[11] C. E. Colosqui, M. J. Cheah, I. G. Kevrekidis, J. Benziger, Droplet and Slug Formation in Polymer Electrolyte Membrane Fuel Cell Flow Channels: The Role of Interfacial Forces. J. Power Sources, 196 (2011) 10057–10068.

[12] L. S. Ferreira, J. O. Trierweiler, Modeling and Simulation of the Polymeric Nanocapsule Formation Process. IFAC Proc., 7 (2009) 405–410.

13] G. He, P. Ming, Z. Zhao, A. Abudula, Y. A. Xiao, Two-Fluid Model for Two-Phase Flow in PEMFCs. J. Power Sources, 163 (2007) 864–873.

[14] A. Bazylak, Liquid Water Visualization in PEM Fuel Cells: A Review. Int. J. Hydrogen Energy, 34 (2009) 3845–3857.

[15] J. Park, X. Li, D. Tran, T. Abdel-Baset, D. S. Hussey, D. L. Jacobson, M. Arif. Neutron Imaging Investigation of Liquid Water Distribution in and the Performance of a PEM Fuel Cell. Int. J. Hydrogen Energy, 33 (2008) 3373–3384.

[16] A. Iranzo, P. Boillat, Liquid Water Distribution Patterns Featuring Back-Diffusion Transport in a PEM Fuel Cell with Neutron Imaging. Int. J. Hydrogen Energy, 39 (2014) 17240–17245.

[17] M. Strobl, I. Manke, N. Kardjilov, A. Hilger, M. Dawson, J. Banhart, Advances in Neutron Radiography and Tomography. J. Phys. D. Appl. Phys., 42 (2009) 243001.

[18] N. Pekula, K. Heller, P. Chuang, A. Turhan, M. Mench, J. Brenizer, K. Ünlü, Study of Water Distribution and Transport in a Polymer Electrolyte Fuel Cell Using Neutron Imaging. Nucl. Instruments Methods Phys. Res., 542 (2005) 134–141.

[19] R. Satija, D. L. Jacobson, M. Arif, Werner, S. A. In Situ Neutron Imaging Technique for Evaluation of Water Management Systems in Operating PEM Fuel Cells. J. Power Sources, 129 (2004) 238–245.

[20] A. Iranzo, P. Boillat, J. Biesdorf, E. Tapia, A. Salva, Guerra, J. Liquid Water Preferential Accumulation in Channels of PEM Fuel Cells with Multiple Serpentine Flow Fields. Int. J. Hydrogen Energy, 39 (2014) 15687–15695.

[21] K. Ogawa, T. Haishi, M. Aoki, Hasegawa, H.; Morisaka, S.; Hashimoto, S. NMR Measurement System Including Two Synchronized Ring Buffers, with 128 Rf Coils for in Situ Water Monitoring in a Polymer Electrolyte Fuel Cell. Rev. Sci. Instrum., 88 (2017) 14701.

[22] G. J. Rees, S. T. Orr, L. O. Barrett, J. M. Fisher, J. Houghton, G. H. Spikes, B. Theobald, D. Thompsett, M. E. Smith, J. V. Hanna, Characterisation of Platinum-Based Fuel Cell Catalyst Materials Using 195Pt Wideline Solid State NMR. Phys. Chem. Chem. Phys., 15 (2013) 17195–17207.

[23] K. W. Feindel, L. P. Larocque, D. Starke, S. H. Bergens, R. E. Wasylishen, In Situ Observations of Water Production and Distribution in an Operating H 2 / O 2 PEM Fuel Cell Assembly Using 1 H NMR Microscopy. J. Am. Chem. Soc., 126 (2004) 11436–11437.

[24] S. Tsushima, K. Teranishi, S. Hirai, Water Diffusion Measurement in Fuel-Cell SPE Membrane by NMR. Energy, 30 (2005) 235–245.

[25] K. R. Minard, V. V. Viswanathan, P. D. Majors, Wang, L. Q.; Rieke, P. C. Magnetic Resonance Imaging (MRI) of PEM Dehydration and Gas Manifold Flooding during Continuous Fuel Cell Operation. J. Power Sources, 161 (2006) 856–863.

[26] R. Banerjee, S. G. Kandlikar, Liquid Water Quantification in the Cathode Side Gas

Channels of a Proton Exchange Membrane Fuel Cell through Two-Phase Flow Visualization. J. Power Sources, 247 (2014) 9–19.

[27] Q. Dong, J. Kull, M. M. Mench, Real-Time Water Distribution in a Polymer Electrolyte Fuel Cell. J. Power Sources, 139 (2005) 106–114.

[28] H. Guo, X. Liu, J. F. Zhao, F. Ye, C. F. Ma, Effect of Low Gravity on Water Removal inside Proton Exchange Membrane Fuel Cells (PEMFCs) with Different Flow Channel Configurations. Energy, 112 (2016) 926–934.

[29] H. Guo, X. Liu, J. F. Zhao, C. F. Ye, F.; Ma, Experimental Study of Two-Phase Flow in a Proton Exchange Membrane Fuel Cell in Short-Term Microgravity Condition. Appl. Energy, 136 (2014) 509–518.

[30] K. Tüber, D. Pócza, C. Hebling, Visualization of Water Buildup in the Cathode of a Transparent PEM Fuel Cell. J. Power Sources, 124 (2003) 403–414.

[31] E. Gauthier, T. Hellstern, I. G. Kevrekidis, J. Benziger, Drop Detachment and Motion on Fuel Cell Electrode Materials. ACS Appl. Mater. Interfaces, 4 (2012) 761–771.

[32] I. Manke, C. Hartnig, M. Grunerbel, W. Lehnert, N. Kardjilov, A. Haibel, A. Hilger, J. Banhart, H. Riesemeier, Investigation of Water Evolution and Transport in Fuel Cells with High Resolution Synchrotron X-Ray Radiography. Appl. Phys. Lett., 90 (2007) 174105+3.

[33] J. Hinebaugh, J. Lee, A. Bazylak, Visualizing Liquid Water Evolution in a PEM Fuel Cell Using Synchrotron X-Ray Radiography. J. Electrochem. Soc., 159 (2012) F826–F830.

[34] T. Mukaide, S. Mogi, J. Yamamoto, A. Morita, S. Koji, K. Takada, K. Uesugi, K. Kajiwara, T. Noma, In Situ Observation of Water Distribution and Behaviour in a Polymer Electrolyte Fuel Cell by Synchrotron X-Ray Imaging. J. Synchrotron Radiat., 15 (2008) 329–334.

[35] G. Minor, Flow within a Water Droplet Subjected to an Air Stream in a Hydrophobic

Microchannel. Fluid Dyn. Res., 41 (2009) 45506.

[36] M. Mortazavi, K. Tajiri, Effect of the PTFE Content in the Gas Diffusion Layer on Water Transport in Polymer Electrolyte Fuel Cells (PEFCs). J. Power Sources, 245 (2014) 236–244.

[37] X. G. Yang, F. Y. Zhang, A. L. Lubawy, C. Y. Wang, Visualization of Liquid Water Transport in a PEFC. Electrochem. Solid-State Lett., 7 (2004) A408–A411.

[38] A. Bazylak, D. Sinton, N. Djilali, Dynamic Water Transport and Droplet Emergence in PEMFC Gas Diffusion Layers. J. Power Sources, 176 (2008) 240–246.

[39] J. Bachman, A. Santamaria, H. Tang, J. W. Park, Investigation of Polymer Electrolyte Membrane Fuel Cell Parallel Flow Field with Induced Cross Flow. J. Power Sources, 198 (2012) 143–148.

[40] J. Lee, J. Hinebaugh, A. Bazylak, Synchrotron X-Ray Radiographic Investigations of Liquid Water Transport Behavior in a PEMFC with MPL-Coated GDLs. J. Power Sources, 227 (2013) 123–130.

[41] I. Manke, C. Hartnig, M. Grünerbel, W. Lehnert, N. Kardjilov, A. Haibel, A. Hilger, J. Banhart, H. Riesemeier, Investigation of Water Evolution and Transport in Fuel Cells with High Resolution Synchrotron X-Ray Radiography. Appl. Phys. Lett., 90 (2007) 174105.

[42] J. Hinebaugh, P Challa, A. Bazylak, Accounting for Low-Frequency Synchrotron X-Ray Beam Position Fluctuations for Dynamic Visualizations. J. Synchrotron Radiat., 19 (2012) 994–1000.

[43] C. A. Rulison, Practical Comparison Of The Techniques Used To Measure Contact Angles For Liquids On Non-Porous Solids, technical note TN303e, Chemical, Pharma, Automotive, Paint, Energy, Polymer, Construction, (1996) 1–8.

[44] K. Chen, M. Hickner, D. Noble, Simplified Models for Predicting the Onset of Liquid Water Droplet Instability at the Gas Diffusion Layer / Gas Flow Channel Interface. Int. J. Energy Res., 29 (2005) 1113–1132.

[45] P. Rahimian, R. Anderson, L. Zhang, Predictions of Flow Regimes in Proton Exchange Membrane Fuel Cells: An Analytical Approach. Int. J. Hydrogen Energy, 42 (2017) 4679–4689.

Chapter 5 - Conclusions and recommendations

5.1 Summary of results

An analytical method was used to predict the two-phase flow regimes in the gas flow channels of fuel cells. Based on three different data sets obtained from active fuel cells, the critical detachment size of droplets was calculated using a force balance analysis. The critical detachment diameter of the droplets decreased with increasing gas velocity and particularly at lower gas velocities this effect became more noticeable. The critical droplet size was also found to be a function of contact angle and contact angle hysteresis. Any increase in contact angle resulted in a decrease in critical droplet size while increasing contact angle hysteresis led to an increase in critical droplet size. This indicated the fact that smaller droplets could detach from more hydrophobic surfaces.

The force estimates to determine the onset of slug, droplet, and film flow showed that the forces needed to remove slugs was higher than forces required for droplet motion. This result is due to the obstruction of whole cross-sectional area of the gas flow channel via slugs which produces high flow resistance. Using critical droplet diameters as an input for a flow regime assignment procedure, a flow regime map was produced. Generally, slug flow mainly forms at low superficial velocities. Film/droplet flow can be seen at higher superficial velocities which corresponded to higher current densities. Single-phase flow occurs at low liquid velocities and high gas velocities corresponding to high gas stoichiometry. Stagnant flow occurs at very low current densities when the water production rate is very low and it take a long time for droplets to reach to the critical size to detach. There was a reasonable qualitive agreement with flow regime maps. The agreement was

best for the slug flow prediction while there was some scatter between the droplet/film flow and single-phase flow regimes.

Regarding the experimental approach, time dependent droplet dynamics in gas flow channels were explored with synchrotron X-ray imaging. The evolution of the dynamic contact angles of growing droplets was visualized. At low superficial gas velocity (4.2 m/s), during the evolution of advancing and receding contact angles, four different phases were detected from captured X-ray images. However, at high superficial gas velocity (10.3 m/s), growing droplets had a fixed shape for a long period of time, experiencing two phases during emergence up to the detachment.

A cyclic pattern for evolution of the height and chord of an emerging droplet was detected. X-ray images reveal that stick-slip contact line motion of unstable droplets correlates with the dynamic contact angles of droplets. By increasing superficial gas velocity from 4.2 m/s to 10.3 m/s, the critical detachment diameter of the droplets decreased from 0.49 mm to 0.25 mm. By increasing the gas velocity, the droplet height against chord decreased close to 0.5 indicating that droplets become more hemispherical at higher superficial gas velocities. Also, increasing gas velocity from 4.2 m/s to 10.3 m/s causes the contact angle hysteresis of detaching droplets to decrease since droplets with larger critical size deform more due to larger differential pressure forces between the upstream and downstream surfaces of the droplet.

5.2 Conclusions

1- The evaluations of the Damkohler number shows the dependence of D_{a0} on air relative humidity and current density. By increasing current density, water production rate increases which leads to an increase in D_{a0}. Also, D_{a0} increases significantly when increasing relative humidity due to decreased water removal via diffusivity.

2- The critical droplet diameter defines two regions for droplets: stable and unstable. Droplets below the critical droplet size are regarded as stable while droplets above the critical droplet size are unstable and detach from the GDL surface. The critical detachment diameter of droplets depends on superficial air velocity, contact angle and contact angle hysteresis.

3- The flow regime is also determined by the contact angle and the magnitude of the contact angle hysteresis. When the contact angle hysteresis grows, slug flow is more probable to occur in the gas flow channel of a PEM fuel cell.

4- X-ray images show that the critical detachment the diameter of the droplets decreases when increasing the superficial gas velocity.

5- It is indicated that increasing the superficial gas velocity results in a decrease in both contact angle hysteresis and droplet aspect ratio making the shape of detaching droplets more symmetrical and spherical. This observation indicates that the assumption of hemispherical droplets in simplified models is more realistic at high superficial gas velocities.

6- It is found that the dimensionless droplet height depends on the contact angle hysteresis of the growing droplets. As droplets grow they block more cross-sectional area of the channel. Hence, droplets deform due to the pressure difference between the upstream and downstream sides of the droplet.

7- X-ray images indicate that increasing gas flow rate expands the droplet-instability window and thus facilitates water removal.

5.3 Recommendations

In this study, a force balance analysis is proposed to predict which flow regime is probable to occur in the gas flow channels of the cell. However, the force balance analysis was only conducted on a single droplet in the channel. In actual conditions in operating cells, multiple droplets emerge simultaneously along the flow channel. When one droplet detaches from the surface of the GDL, it might combine with more droplets downstream and make larger droplets. This phenomenon is not considered in this study. Therefore, the effect of multiple droplet growth on the flow regime assignment should be investigated in the future work.

The water balance in PEM fuel cells is a complex phenomenon. The parameters studied for the flow regime assignment in the analytical approach included superficial gas velocity, contact angle and contact angle hysteresis. The analysis here does not consider the impact of temperature, relative humidity and GDL properties (thickness, porosity, etc.) which should be explored in the future studies.

In the experimental approach, the effect of other factors such as dynamic injection ports, differentiation of GDLs with and without MPL, and possible condensation/evaporation on the droplet growth cycle should be explored using X-ray radiography.

X-ray images revealed that the height to chord ratio of the droplet decreased to 0.5 by increasing the superficial gas velocity. Hence, at low gas velocities, the hemispherical droplet assumptions needs to be revisited in simulations and simplified models.

In addition to water management applications in PEM fuel cells, the results presented here can be extended to some other microfluidic devices with an emphasis on droplet dynamics where optical access is demanding.

Appendix A - Flow patterns observed from X-ray imaging techniques

In previous work, an analytical approach to estimate the flow patterns in an operating PEMFC was developed based on a force balance analysis and finally an expected flow regime map was assigned [1]. As it is shown in Figure A.1, the former flow regime map has been updated with results obtained from synchrotron X-ray visualization data.

In general, there is a good qualitative agreement between recent experimental results and the previous flow pattern based on operating conditions of Anderson et al. [2], Hussaini and Wang [3] and See [4]. Solid lines indicate the flow pattern boundary estimations using empirical correlations which was proposed by Hussaini and Wang [5]. In general, two-phase flow in the flow channels of fuel cells can be categorized into three main flow patterns, namely, slug flow, droplet/film flow, and single-phase flow.

At low superficial gas velocity where drag force for removing liquid water is minimal, mainly slug flow is observed. As seen in Figure A.2, as the time goes by stagnant slugs grow larger due to the constant flow of water though the pores of the GDL and getting merged with other droplets in the channel. Large stagnant slugs can block the cross section of the channel and consequently increase the probability of channel flooding. To remedy the situation, PTFE coating is used which makes the GDL surface hydrophobic. As can bee seen in Figure A.2, the resultant difference in hydrophobicity with the channel side walls makes trapezoidal shaped slugs which occupy a smaller area of the GDL surface and increase the passage of reactants to the catalyst layer.

At higher superficial gas velocities corresponding to higher current densities, droplet/film flow is observed. During the droplet flow regime, small drops emerge at the interface of the GDL and the channel and grow gradually while they are pinned to the GDL surface. After reaching to a

critical diameter they shear off the surface via the drag force of the gas flow. By further increasing the superficial water velocity, increased number of emerging droplets makes an elongated rippling water film.

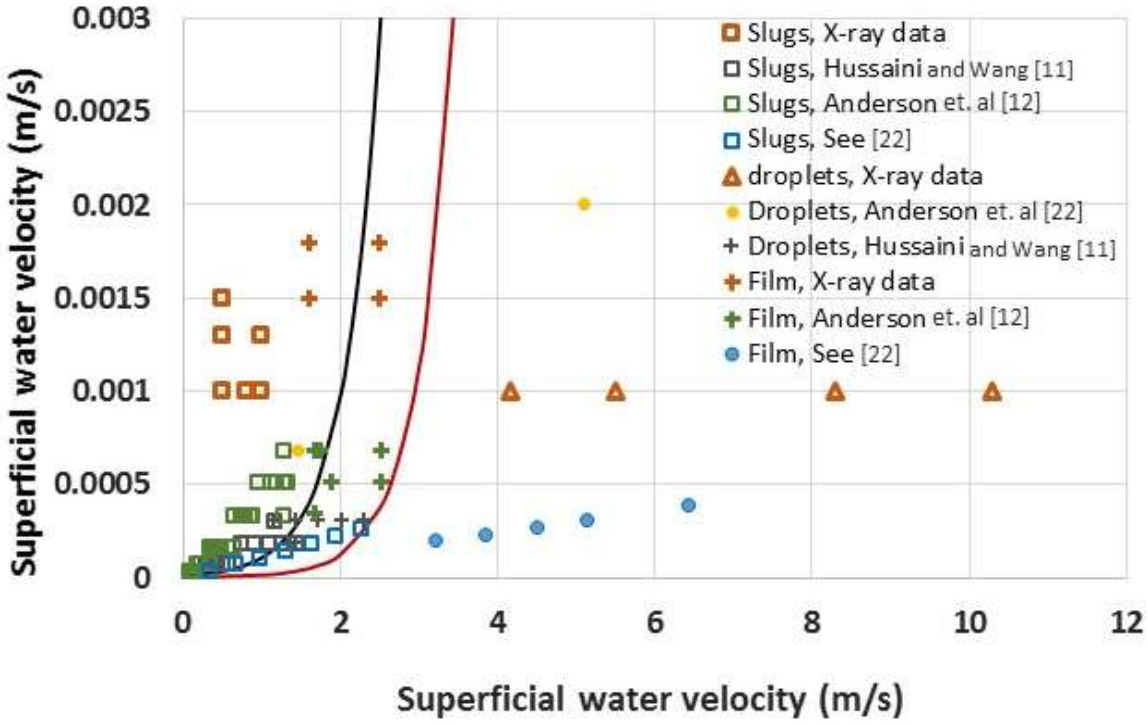

Figure A.1 flow map of different flow patterns in gas flow channel of a model fuel cell as observed.

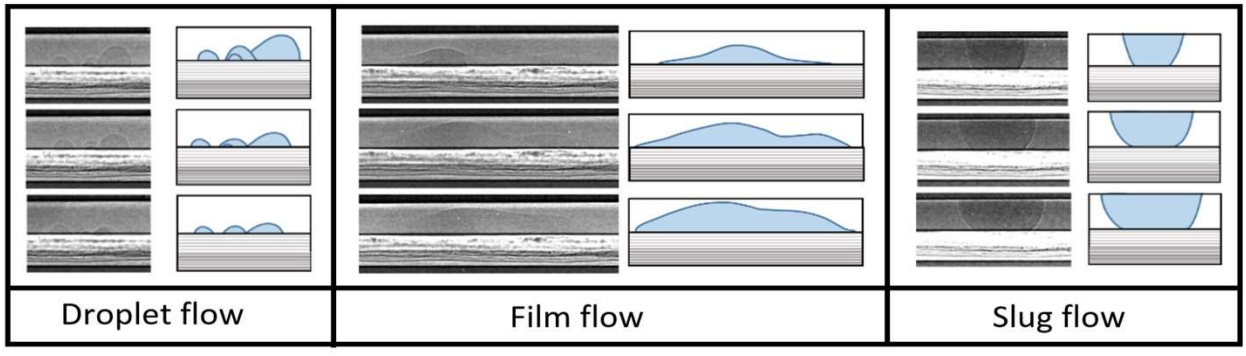

Figure A.2 Typical flow regimes in a gas flow channel of a model fuel cell.

A.1 References

[1] P. Rahimian, R. Anderson, and L. Zhang, Predictions of flow regimes in proton exchange membrane fuel cells: An analytical approach, Int. J. Hydrogen Energy. 42 (2017) 4679–4689.

[2] R. Anderson, D. P. Wilkinson, X. Bi, L. Zhang, Two-phase flow pressure drop hysteresis in an operating proton exchange membrane fuel cell, J. Power Sources. 196 (2011) 8031-8040.

[3] I. S. Hussaini, C. Y. Wang, Visualization and quantification of cathode channel flooding in PEM fuel cells, J. Power Sources. 187 (2009) 444-451.

[4] E. See, In situ measurement, characterization, and modeling of two-phase pressure drop incorporating local water saturation in PEMFC gas channels, Rochester Institute of Technology, Troy, NY (2013).

[5] I.S. Hussaini, C.Y. Wang, Visualization and quantification of cathode channel flooding in PEM fuel cells, J. Power Sources. 187 (2009) 444–451.

Appendix B - Droplet behavior touching corners at low gas velocities

According to Zhang et al. 's [1] classification, there are two possible modes to remove liquid water from the GDL depending on superficial gas velocity and liquid water production rate. At high gas velocity, drag force exerted by the gas flow can overcome the adhesion force and consequently the droplet can detach from the GDL surface. When the gas velocity is low, capillary interactions result in water spreading over hydrophilic channel walls and drain via corner flow through the edges of flow channels. At higher water flow rates, film flow takes the place of corner flow in gas flow channels. Many researchers have used the Concus and Finn model, which provides a good understanding of liquid water behavior touching two surfaces of different contact angles [2],

$$\theta_B + \theta_w \geq \pi + 2\alpha \tag{B.1}$$

Where α is open angle of the channel edge. According to equation B.1, if the contact angle that a droplet makes with the channel wall (θ_w) plus the contact angle of the droplet with base GDL (θ_B) is larger than ($\pi + 2\alpha$), liquid water can wet the channel corner and then corner flow occurs. Using the above equation, droplet behaviour on the GDL and channel walls are divided into two types of interactions, filling and non-filling. Droplet interactions with hydrophobic GDL surface and hydrophilic side wall of channel are shown in Figure B.1. It shows a sequence of close up X-ray images indicating droplet emergence on the GDL surface (CH1, t: 1 s – 14 s), water drainage by corner flow (CH1, t: 1 s – 189 s) and formation of film flow (CH2, t: 1 s – 189 s). At low superficial air velocity (2.5 m/s), small droplets are emerging and growing on the GDL surface between 1 s and 14 s in CH1. At the same time, hydrophilic channel walls drain liquid water via corner flow and fill the left corner of CH1. This filled corner acts as a wetted site for new emerging

droplets and attracts them toward the corner side of the channel. They coalesce to the existing corner flow and continuously accumulate on the left sidewall of CH1. With time, continuous water accumulation makes corner flow larger until it slowly spreads and forms a thin layer of film on the channel sidewall. In the same way, due to the different hydrophobicity of GDL base and channel walls, film flow is the dominant flow pattern in CH2 and CH3. In Image 3 it can be observed that a small droplet emerges from the pores of GDL and subsequently merges to the thick layer of liquid water film covering the side wall on the right side of CH2. This clearly elucidates how droplet pinning in the corners via capillary forces leads to corner flow and consequently annular film flow alongside the channel walls that attracts small emerging droplets towards the growing film flow. As Zhu et al. [3] mentioned, constant growth of liquid water film obstructed the pores of GDLs, the reactant pathways, and thus reduced the cell performance. In case of high water flow rate and low gas velocity, the thickness of film flow increases to a critical size that any further growth lead to formation of slow-moving slugs. This will subsequently cause oscillation in pressure and voltage signals [4].

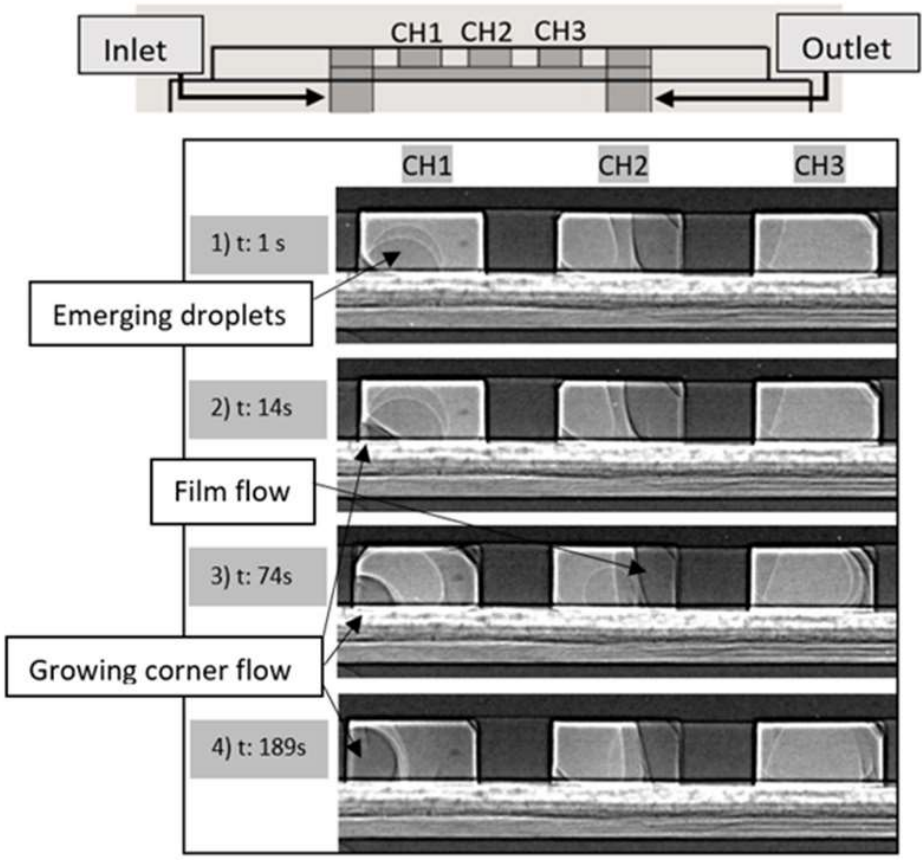

Figure B.1 X-ray images showing liquid water corner flow at air velocity of 2.5 m/s with hydrophilic channel walls in a serpentine channel (cross sectional view).

From sequential X-ray images obtained from experiments, instantaneous dynamic contact angles droplets made with both base GDL and channel wall surfaces were measured. A plot was constructed according to the Concus-Finn relation discussed above. The results are shown in Figure B.2. The red solid line shows the theoretical Concus–Finn limit line ($\theta_B + \theta_W = 270°$).

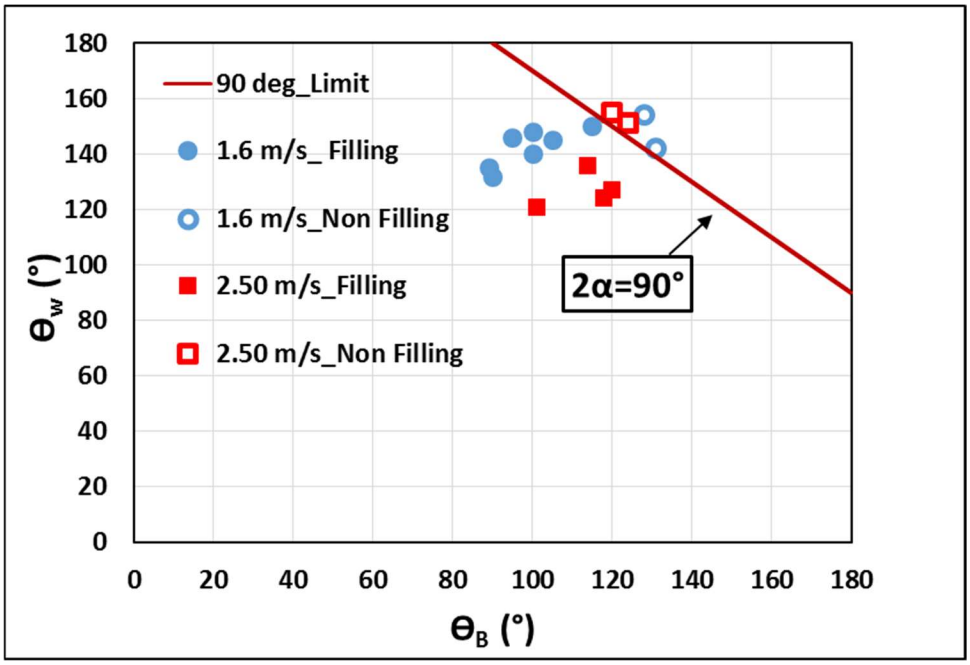

Figure B.2 Dynamic contact angles of droplets made with base GDL and hydrophilic channel walls at different air velocities. Red solid line is theoretical Concus-Finn limit line for 90° open angle gas flow channel.

It can be seen in this figure that even if one of contact angles falls below the Concus–Finn limit line, the droplet would touch the corner of the flow channel. Figure B.2 shows the instantaneous dynamic contact angles for a rectangular channel (90° open angle) at two different superficial air velocities (u_g = 2.5 m/s and 1.6 m/s). In this figure, some droplet contact angle points obtained from X-ray images fell below the Concus–Finn limit line, indicating that the droplets forming in gas flow channels of our experimental test cell can fill the 90° channel corners at low gas velocities.

B.1 References

[1] F.Y. Zhang, X.G. Yang, C.Y. Wang, Liquid Water Removal from a Polymer Electrolyte Fuel Cell, J. Electrochem. Soc. 153 (2006) A225.

[2] K.S. Chen, M.A. Hickner, D.R. Noble, Simplified models for predicting the onset of liquid water droplet instability at the gas diffusion layer / gas flow channel interface, Int. J. Energy Res. 29 (2005) 1113–1132.

[3] X. Zhu, P.C. Sui, N. Djilali, Three-dimensional numerical simulations of water droplet dynamics in a PEMFC gas channel, J. Power Sources. 181 (2008) 101–115.

[4] K.R. Minard, V. V. Viswanathan, P.D. Majors, L.Q. Wang, P.C. Rieke, Magnetic resonance imaging (MRI) of PEM dehydration and gas manifold flooding during continuous fuel cell operation, J. Power Sources. 161 (2006) 856–863.

Appendix C - Contact angle measurement

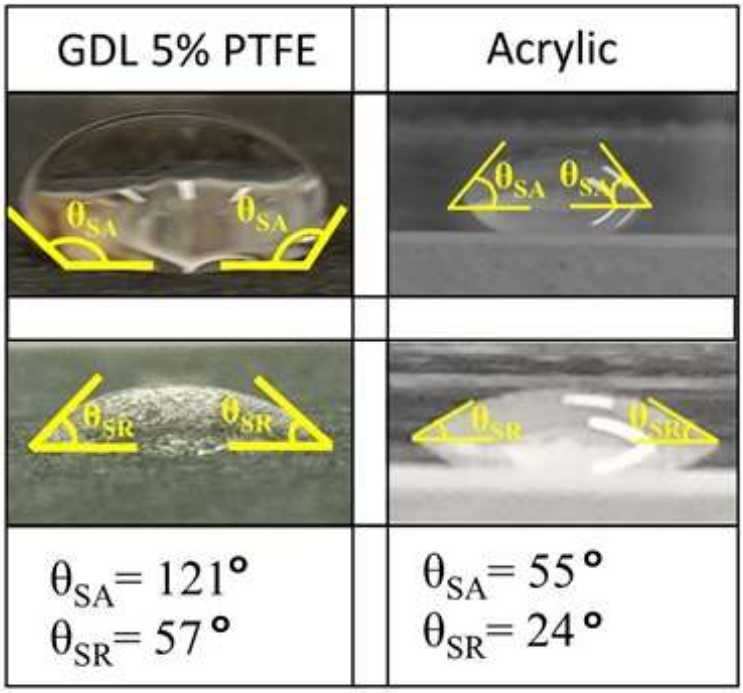

Figure C.1 Static contact angle measurement for GDL with 5% loaded PTFE and acrylic.

In order to measure contact angles, Goniometer method was used. This method allows user to measure advancing and receding contact angles of droplet visually. A droplet was placed above sample surface using a syringe so that a high-resolution camera can capture side view images from the droplet. Thereafter, captured images were analysed using ImageJ. This type of measurement is termed static contact angle measurement. In order to measure dynamic contact angle hysteresis, the volume of sessile droplet is gradually increased and the maximum possible contact angle is termed advancing contact angle. Similarly, receding contact angle is obtained by decreasing the volume of sessile droplet and the minimum possible contact angle is termed receding contact angle. The difference between advancing and receding contact angles is termed contact angle hysteresis.

Appendix D - Acrylic fuel cell in the beamline

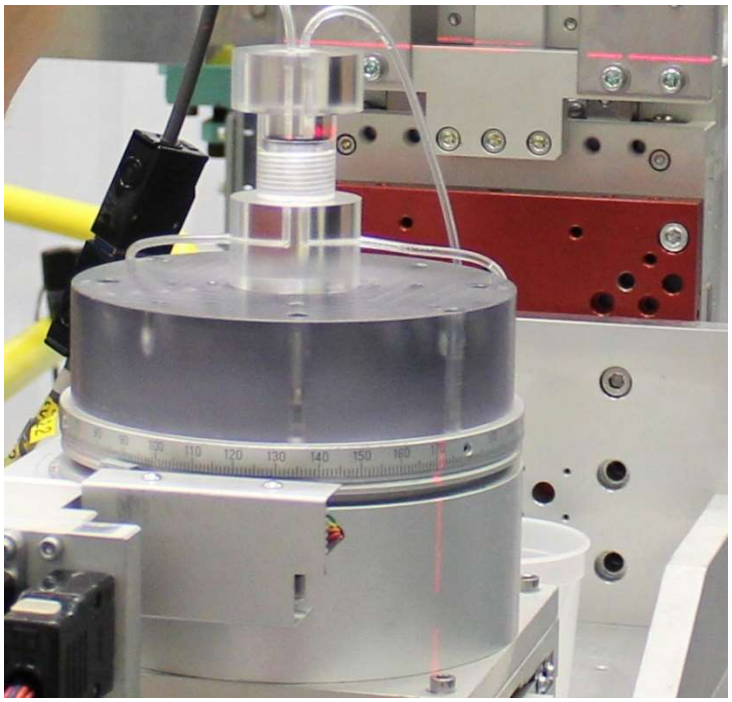

Figure D.1 Acrylic fuel cell mounted on stage in BMIT beamline at the CLS.

Appendix E – Uncertainty of experiments

In order to control the water flow rate, a syringe pump (New Era Pump Systems, Inc) was used. The accuracy of the syringe pomp with a maximum flow rate of 35.33 mL/min was +/-1%. Also, a mass flow meter (FL-3802ST, Omega, Canada) was used to control the air flow rate with the accuracy of +/-2% of the full scale of 814 ml/min. The measurements of critical droplet diameters were repeated three times and the relative error of each condition is reported in Table E.1.

Table E.1 Uncertainty of critical droplet diameter measurements from X-ray images.

Superficial gas velocity, m/s	Critical droplet diameter, mm	Relative error, %
4.2	0.49	4
5.5	0.41	7
8.3	0.32	5
10.3	0.25	7

Appendix F – Solid work scheme

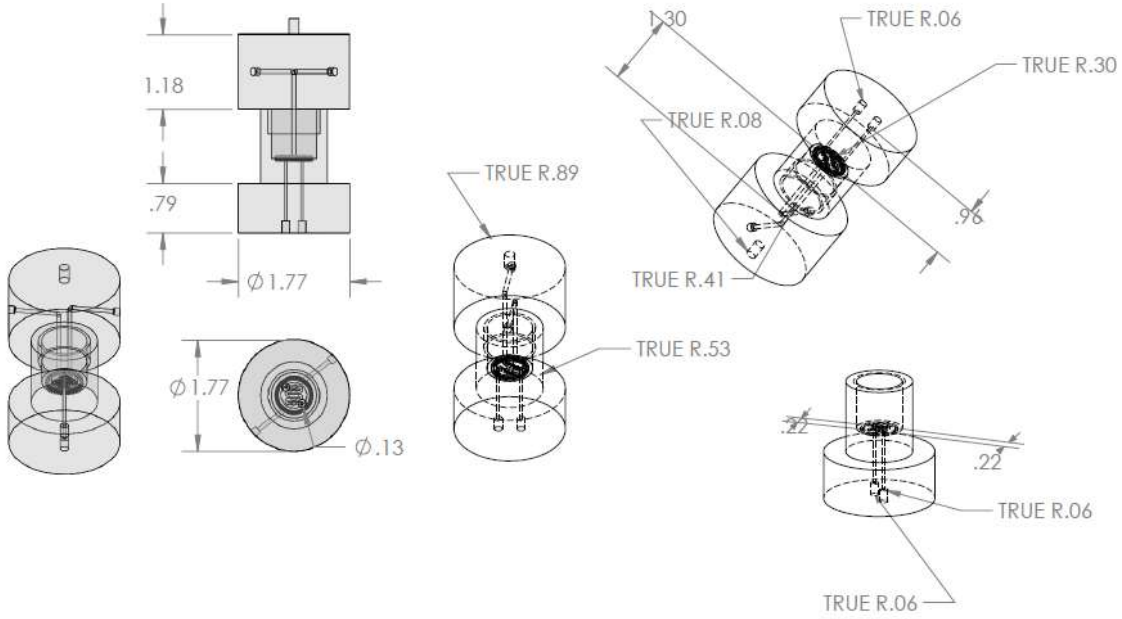

Figure F.1 Solid work scheme of the acrylic test fuel cell.

Appendix G – Copyright firms

9/7/2017 RightsLink Printable Job Ticket

ELSEVIER ORDER DETAILS

Sep 07, 2017

Order Number	501306356
Order date	Sep 07, 2017
Licensed Content Publisher	Elsevier
Licensed Content Publication	International Journal of Hydrogen Energy
Licensed Content Title	Predictions of flow regimes in proton exchange membrane fuel cells: An analytical approach
Licensed Content Author	Paria Rahimian,Ryan Anderson,Lifeng Zhang
Licensed Content Date	16 February 2017
Licensed Content Volume	42
Licensed Content Issue	7
Licensed Content Pages	11
Start Page	4679
End Page	4689
Type of Use	reuse in a thesis/dissertation
Portion	full article
Format	both print and electronic
Are you the author of this Elsevier article?	Yes
Will you be translating?	No
Title of your thesis/dissertation	Using Synchrotron Based X-Ray Imaging Technique to Understand Liquid Water Transport Phenomena in Proton Exchange Membrane (PEM) Fuel Cells
Expected completion date	Sep 2017
Estimated size (number of pages)	126
Requestor Location	3B48 Engineering Building 57 Campus Drive 57 Campus Drive

Print This Page